Science of Remote Sensing 12 (2025) 100311

Contents lists available at ScienceDirect

Science of Remote Sensing

journal homepage: www.sciencedirect.com/journal/science-of-remote-sensing

Drone-borne ground-penetrating radar reveals spatiotemporal moisture dynamics in peatland root zones

Maud Henrion [a,*], Yanfei Li [a], Kaijun Wu [a], François Jonard [b], Sophie Opfergelt [a], Veerle Vanacker [a], Kristof Van Oost [a], Sébastien Lambot [a]

[a] Earth and Life Institute, Université catholique de Louvain, Louvain-la-Neuve, Belgium
[b] Earth Observation and Ecosystem Modelling Laboratory, Université de Liège, Liège, Belgium

ARTICLE INFO

Keywords:
Peatlands
Proximal soil sensing
Ground-penetrating radar
Drone
Full-wave inversion
Soil moisture
Peatland restoration

ABSTRACT

Peatlands are important ecosystems, providing essential ecological services, such as carbon storage and biodiversity support. However, they are endangered by degradation due to land use and climate change. Their moisture status is a key factor, as it substantially impacts carbon storage and decomposition. Therefore, it is essential to accurately characterize, map, and monitor peatland moisture. This study assessed the potential of drone-borne Ground-penetrating radar (GPR), combined with full-wave inversion, to study peatland moisture. We applied this technique to a peatland in the Belgian Hautes Fagnes previously degraded by reforestation. We conducted GPR measurements over 4.5 ha for one and a half years, producing 19 different peatland root-zone moisture maps at a 5 m resolution. Our results demonstrate that this method can track moisture changes over the study site, with an overall temporal correlation of 0.71 with ground-based moisture sensors, but is less reliable in nearly saturated areas. The spatial correlation with ground-based probes is lower (0.23), due to the high micro-variability of moisture and the use of kriging interpolation to generate maps, resulting in a spatial mismatch as GPR measurements were not collected directly above the probes. We applied statistical clustering techniques on the moisture maps to delineate homogeneous moisture classes that align well with other specific site characteristics (peat depth, vegetation types, Normalized Difference Water Index and surface temperature). This technique shows potential for planning and monitoring peatland restoration efforts and provides a new and valuable approach for peatland moisture studies to complement existing satellite- and other drone-based methods.

1. Introduction

Peatlands contain nearly 30 % of the global soil carbon stock, which corresponds to twice the amount of carbon stored in the entire forest biomass (UNEP, 2022). They are also crucial for biodiversity support, water storage and filtration, and cultural services (Saarikoski et al., 2019). About 12 % of peatland ecosystems are degraded worldwide due to agriculture, forestry, and other uses. Peatland degradation is particularly problematic in Europe, where almost 50 % of peatlands are degraded (UNEP, 2022). They are often drained, which results in water table lowering, increased aeration, and subsequent mineralization of organic matter (Holden et al., 2004). Peatland drainage contributes to 4 % of the annual anthropogenic greenhouse gases emissions (UNEP, 2022).

Peatland restoration initiatives now aim to restore degraded peatlands back to their original conditions to allow them to regain their important functions (Gorham and Rochefort, 2003). These initiatives are not only costly, they are also complex to implement, and do not always allow to restore the original ecosystem characteristics (Kreyling et al., 2021). In Europe, some projects were launched with the objective of promoting peatland restoration initiatives, among other goals, such as the EU-Life Nature program in 1992 (Andersen et al., 2017) and the EU Mission 'A Soil Deal for Europe' in 2021 (European Commission, 2021). Common restoration practices include raising water table levels and facilitating the growth of peat-forming mosses such as *Sphagnum* (Holden et al., 2004). In their studies, Andersen et al. (2017) and Minasny et al. (2023) emphasized the need to monitor peatlands both before restoration initiatives are implemented, to ensure proper planning, and

Abbreviations: GPR, Ground-penetrating radar; *VWC*, volumetric water content; NDWI, Normalized Difference Water Index; TWI, Topographic Wetness Index.

* Corresponding author. Earth and Life Institute, Université catholique de Louvain, Croix du Sud 2, 1348, Louvain-la-Neuve, Belgium.
E-mail addresses: maud.henrion@uclouvain.be (M. Henrion), sebastien.lambot@uclouvain.be (S. Lambot).

https://doi.org/10.1016/j.srs.2025.100311
Received 17 February 2025; Received in revised form 22 August 2025; Accepted 9 October 2025
Available online 10 October 2025

afterward, to assess their success. However, this has rarely been done in Western European projects to date, due to limited budgets or short-term project definitions (Allan et al., 2024). Common indicators used to assess restoration success include vegetation composition (González et al., 2014) and water table depth (Menberu et al., 2016).

Soil moisture status is a key parameter in peatlands, as waterlogged conditions slow down plant decomposition and facilitate carbon storage. Peatlands are ecosystems prone to water-saturation and characterized by overland flow and preferential pathways (Holden, 2006). Moisture levels in peatlands usually exhibit large spatial variability, with spatial patterns differing between wet and dry periods (Petrone et al., 2004). The spatial variation in peatland soil moisture is influenced by large-scale variations in geomorphology and geology, as well as smaller-scale variations in vegetation, microtopography (Petrone et al., 2004), and hydraulic properties (Wang et al., 2021). In terms of temporal variability, moisture changes are primarily driven by weather conditions (Bourgault et al., 2019). Besides weather-related seasonal changes, water table fluctuations tend to be moderate in response to external drying and wetting events (Waddington et al., 2015; Wastiaux, 2008). Soil moisture levels in peatlands are closely linked to water table depth (Price, 1997) but exhibit greater spatial heterogeneity. Studying soil moisture rather than water table depth offers several complementary benefits, as this variable is more responsive to weather conditions, better reflects actual water availability (Price, 1997), and is more directly linked to microbial activity (Kechavarzi et al., 2010).

A variety of techniques exist to characterize peatland moisture over various spatial and temporal scales. Firstly, satellite data are often used to estimate water table depth in peatlands. Although water table depth is not directly observed by satellite sensors, it can be inferred from several surface indicators. Water table depth is preferred over soil moisture in satellite-based peatland studies because it exhibits lower spatial variability and is therefore more suitable for large-scale estimation, while remaining closely related to near-surface soil moisture. Optical satellite imagery allows for the computation of vegetation-related indices that provide information on moisture status, given the strong correlation between botanical and hydrological indicators in peatlands (Linkevičienė et al., 2023). Simple indices based on vegetation phenology, such as the NDVI (Normalized Difference Vegetation Index) and the NDWI (Normalized Difference Water Index), have shown good results (Linkevičienė et al., 2023; Šimanauskienė et al., 2019). More complex indices, such as OPTRAM (Optical Trapezoïd Model; Sadeghi et al., 2017), have also shown significant correlation with peatland water table depth over time (Burdun et al., 2020). Additionally, radar satellites have also demonstrated significant correlation with water table depths in peatlands (Asmuβ et al., 2019; Hrysiewicz et al., 2023). Satellite-based methods yield data over large areas with a frequent but uncontrollable revisit time. However, they have several limitations: limited resolution, limited measurement depth (e.g., less than 5 cm for L-band radar and even less for other satellite remote sensing methods), reduced effectiveness in the case of deeper water tables, and the presence of clouds and vegetation, which can affect the success of optically-based methods (Asmuβ et al., 2019; Burdun et al., 2020, 2023). Secondly, field-scale probes can be used to measure water content. Time Domain Reflectometry (TDR) sensors are commonly used to determine soil water content based on the dielectric constant (Topp and Davis, 1985). However, peat soils require specific calibrations because of their high porosity (Kellner and Lundin, 2001; Pepin et al., 1992). These sensors allow for high temporal resolution monitoring of water content when permanently installed. Nevertheless, their measurements are limited to small spatial scales and may not be representative at larger scales, as interpolation is challenging due to the high inherent soil variability in peatlands.

More recently, drone-borne sensors have been employed to determine soil water content. These sensors bridge the gap between the broader spatial scales of satellites and the finer resolutions of field probes. They offer higher resolution than satellites and provide more controllable revisit times. First, land surface temperature has been shown to correlate well with water table depth in peatlands (Kameoka et al., 2021; Lendzioch et al., 2021). Then, several studies have combined multispectral and thermal data to predict water content or water table depth. For instance, indices such as the TVDI (Temperature Vegetation Dryness Index; Sandholt et al., 2002) have proven successful (Isoaho et al., 2023; Wigmore et al., 2019). More recent drone-based studies have also combined a wider range of remote sensing data with machine learning models to reveal spatial heterogeneities in soil moisture (e.g., Cheng et al., 2022).

Ground-penetrating radar (GPR) is a non-destructive geophysical method that provides high-resolution soil moisture estimates by analyzing wave propagation speed or surface reflection amplitude, both affected by soil permittivity and correlated with moisture levels (Galagedara et al., 2003; Huisman et al., 2003; Klotzsche et al., 2018; Pathirana et al., 2023; Wijewardana and Galagedara, 2010). Using full-wave inversion, which leverages a comprehensive electromagnetic model, GPR enables robust, fully automated soil moisture estimation (Lambot et al., 2004b; Lambot and Andre, 2014). Initial applications of full-wave inversion produced high-resolution soil moisture maps over large areas in agricultural fields using a quad with an off-ground GPR configuration, effectively capturing spatial heterogeneity (Minet et al., 2012). Building on this, studies extended full-wave inversion to drone-borne GPR, enhancing the method's applicability for soil moisture mapping without disturbing soil or vegetation (Wu et al., 2019, 2025). The integration of GPR with drones has expanded its applications in environmental monitoring, such as surface object detection, surface moisture determination, and snowpack estimation (Noviello et al., 2022). For soil moisture mapping, GPR has achieved high accuracy, with reported Root Mean Square Error (RMSE) values below 5 % (Cheng et al., 2023; Pramudita et al., 2022). Despite these advancements, the use of drone-based GPR for soil moisture mapping remains limited, with applications primarily focused on agricultural soils (Cheng et al., 2023; Ding et al., 2023; Pramudita et al., 2022; Wu et al., 2019, 2025).

Given the importance of soil moisture in regulating carbon fluxes, accurately monitoring peatland moisture status is essential, especially for restoration efforts. However, conventional satellite and in situ measurement techniques may lack the spatial representativeness needed to capture peatland moisture variations. This study aims to evaluate the potential of drone-borne GPR for high-resolution mapping and monitoring of root-zone moisture in peatlands. While drone-borne GPR has been validated for agricultural soils, it has not yet been tested in more complex environments like peatlands, which present unique challenges due to high water content, surface roughness, and dense vegetation. The specific objectives of this study are: (1) to apply the drone-borne GPR methodology to peatlands, (2) to assess its potential for monitoring temporal variability in peatland root-zone moisture, (3) to evaluate its capability to identify small- and large-scale spatial moisture patterns, and (4) to discuss its utility in the context of peatland restoration. The study was conducted in a peatland site previously degraded by reforestation in the Belgian Hautes Fagnes, which can be regarded as a typical example of degraded peatlands in this part of Europe. We applied monostatic drone-borne GPR in the 105–125 MHz frequency range, coupled with full-wave inversion, to achieve high-resolution root-zone moisture mapping over time.

2. Methodology

2.1. Study site

The Hautes Fagnes plateau is part of the Stavelot-Venn Massif and is located in the east of Belgium (Goemaere et al., 2016). It is the highest point of Belgium, with an altitude reaching 694 m above sea level. The region experiences a subalpine climate characterized by abundant rainfall (Goemaere et al., 2016). This plateau encompasses the majority of Belgium's peatlands, which are primarily raised bogs (Frankard et al.,

1998). The Hautes Fagnes region is of great ecological interest, rich in water resources and important for tourism (Goemaere et al., 2016). However, many of these peatlands have been degraded by human activities such as peat extraction, drainage and spruce plantation (Frankard, 2004). These degradations are typical for peatlands in this area of Europe (UNEP, 2022). These disturbances have altered the hydrological functioning of the peatlands, leading to the gradual replacement of native plant communities by *Molinia caerulea* (Frankard, 2004). To preserve these important ecosystems, the natural reserve of the Hautes Fagnes was created in 1957. A restoration program began in 1993 with the objective of protecting intact peatlands and restoring degraded ones through various methods including scraping, blocking ditches, rotovating, topsoil removal, flooding with dams, and removing invasive trees (Frankard, 2004). These initiatives have resulted in successful restoration in the areas where they were applied but have proven challenging to implement, costly, and slow regarding the vegetation recolonization (Frankard, 2004).

The entire study site covers an area of 33 ha and is located in the Hautes Fagnes, within the upper valley of the Hoëgne river (Fig. 1). It features a clear topographic gradient with an average slope of 2.2°. Two subzones of interest are indicated in Fig. 1, zone A (2.8 ha) has an average slope of 2.4°, while zone B (1.7 ha) exhibits a steeper slope of 4.6°, these are the places where the GPR measurements were carried out. Historically, the study site was drained for forestry purposes, and spruce trees were planted at the beginning of the 20th century. These trees were cut between 2012 and 2016 as part of the Hautes Fagnes restoration project. Following this, a few hardwood plantations (birch and oak) were established, and the site is now left to its natural evolution. The site can thus be classified as previously degraded and partially restored through a few limited interventions (i.e., spruce clearing). While it differs from natural or fully restored peatlands, it is representative of peatlands at an intermediate stage of restoration in the area. The peat depth on the site varies from 0.2 to 2.1 m, with shallower depths on the slopes (Henrion et al., 2024; Li et al., 2024). The vegetation primarily consists of *Molinia caerulea*, covering 28 % of the surface. Other grasses and shrubs cover 47 % of the surface, while tree species cover 22 % of the surface (Li et al., 2024).

2.2. Drone-borne ground-penetrating radar measurements

2.2.1. Ground-penetrating radar data acquisition

The drone used in this study is a Tundra (Hexadrone, Saint-Ferréol-d'Auroure, France), capable of low-altitude flights with automated terrain-following thanks to a 5 GHz radar rangefinder (Fig. 2). It has a maximum payload capacity of 4 kg and, with the 2 kg radar payload used here, can sustain a flight time of approximately 35 min. The GPR system used is a prototype version of gprSense® (Sensar Consulting, Dion-Valmont, Belgium, https://www.gprsense.com) developed by Sébastien Lambot, with funding from the EU agROBOfood project (MIRAGE, Grant Agreement No. 825395) and the ICAERUS project (gprSense®, Grant Agreement No. 101060643). It integrates a controlling micro-computer, a Vector Network Analyzer (VNA) that sets up a stepped-frequency continuous-wave radar, a Global Positioning System (GPS), and a battery, with a design incorporating lightweight standard components similar to those used in Wu et al. (2019), and a 1-m dipole antenna (Fig. 2). It is controlled via the embedded gprSense® application, accessible through a smartphone via a Wi-Fi hotspot. The use of a dipole antenna allows operation in relatively low-frequency ranges while maintaining a lightweight system (about 2 kg). Additionally, the dipole antenna provides a quasi-isotropic radiation pattern, minimizing influence of the incidence angle variations caused by drone motion (Wu and Lambot, 2022a). In this study, the GPR operated in a frequency range of 105–125 MHz, representing an optimal trade-off between maximizing moisture sensitivity at greater sensing depths and minimizing the influence of soil electrical conductivity (Lambot et al., 2006; Wu and Lambot, 2022b). The resulting characterization depth was

Fig. 2. Drone-borne GPR system. The platform is a Tundra drone (Hexadrone, France), carrying the gprSense® prototype (spring 2023 version, Sensar Consulting, Belgium). The white enclosure houses the battery, micro-computer, and VNA, and the 1-m dipole antenna rods are fixed to the front lower part of the enclosure.

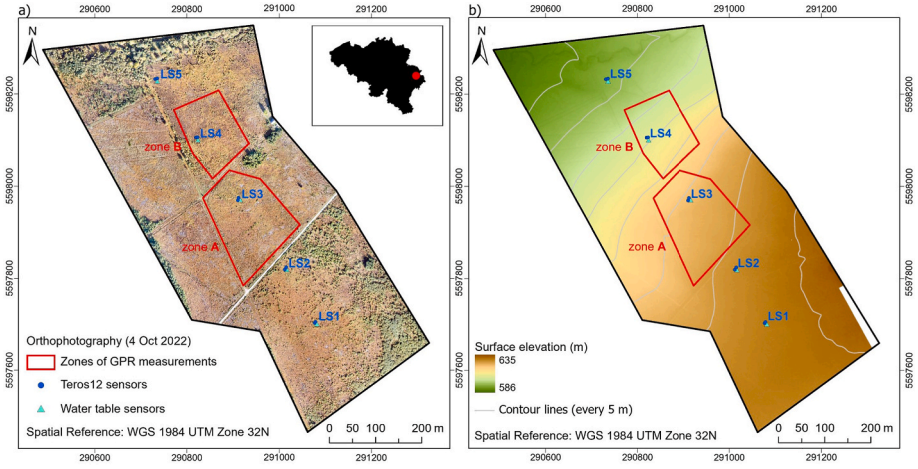

Fig. 1. Location of the study site. The two zones where GPR measurements were taken are indicated, as well as the five topographic positions where volumetric water content (measured with Teros12 sensors) and water table depth are recorded. The dispersed CS615 moisture verification points were collected across the two same zones as the GPR measurements. Thermal and multispectral measurements were conducted over the entire study site. a) Orthomosaic. b) Elevation.

estimated to be the first 35 cm of the subsoil, as determined theoretically by Lambot et al. (2006) and experimentally by Wu et al. (2025). The system collects about 5–10 measurements per second, depending on the radar configuration, with a GPS precision of about 5 m in our case (we did not use a differential GPS). The drone-borne GPR system was calibrated to determine the antenna characteristic functions for the full-wave radar equation of Lambot et al. (2004b) by performing measurements at different heights over a lake.

Two subzones of the study site were surveyed using the drone-borne GPR system (Fig. 1). These subzones were selected for two reasons. First, their relatively low vegetation height (trees <4 m) allowed the GPR to operate closer to the ground, optimizing signal-to-noise ratio. Second, the terrain enabled continuous visual contact with the drone while surveying a sufficiently large area. The two subzones exhibit varying vegetation, topography, and moisture conditions, representative of the entire study site. Measurements were conducted approximately once per month from May 2023 to September 2024, increasing to twice per month during summer due to higher moisture variability, resulting in a total of 19 measurement dates (listed in Table 1). This approach allowed us to capture data over more than a complete meteorological year and across two distinct summer periods. Due to the presence of isolated trees at the study site, manual flights were conducted. Flights were performed at speeds between 1 and 3 m/s and at above-ground heights ranging from 2.5 to 7 m, using the terrain-following mode. It should be noted that higher flight altitude inherently reduces the signal-to-noise ratio. This setup produced a radar measurement every 20–40 cm along the flight path, with flight lines spaced approximately 10 m apart. The resulting volumetric water content (*VWC*) represents the moisture in a 4–5 m^2 footprint, as estimated using the Fresnel zone formula. This footprint is consistent with the 5 m positional accuracy of the GPS used.

2.2.2. Ground-penetrating radar data processing

The radar data were processed using full-wave inversion, focusing on the surface reflection in the time domain (Lambot et al., 2004b, 2006). The full-wave inversion method has previously shown better accuracy in estimating *VWC* compared to the common surface reflection method (Lambot et al., 2006). The radar equation from Lambot et al. (2004b) was employed to describe the radar measurements under far-field conditions, accounting for antenna effects, including radar-medium interactions, and in our case, radar-drone interactions, and 3D wave propagation in planar multilayered media. The theoretical basis of this method was validated by Lambot et al. (2006, 2004b) and Lambot and Andre (2014), then demonstrated high precision in root-zone moisture mapping when carried by a quad or a drone (Minet et al., 2012; Wu et al., 2025). The well-posedness of the inverse problem was demonstrated by Lambot et al. (2004a), and a sensitivity analysis was conducted by Lambot et al. (2006). Uncertainties associated with this method were reported by Lambot et al. (2006) and Minet et al. (2012). The general inversion scheme followed the approach described by Lambot et al. (2006) and Wu et al. (2019), with specific modifications in data processing detailed below. The general GPR processing workflow includes the following steps: (1) GPR data acquisition, (2) radar-drone calibration, (3) full-wave inversion to retrieve soil permittivity, (4) conversion to *VWC,* (5) spatial interpolation (Fig. 3). The electrical conductivity was set to 11 mS/m instead of 0 mS/m. Although this relatively low value does not significantly affect the inversion process, electrical conductivity at this frequency range does slightly influence the surface reflection. Since the average electrical conductivity for our site is known through electromagnetic induction measurements (Henrion et al., 2024), we used this value for improved accuracy in the retrieval process. Soil roughness was also considered, using the method described by Jonard et al. (2019, 2012), as the roughness is relatively large compared to the wavelength according to Rayleigh's criterion. The standard deviation of surface roughness was estimated at 0.1 m based on soil microtopography. A lookup table was created for dielectric permittivity values ranging from 1 to 81, with a step size of 1, and for heights ranging from 2.5 to 7 m, with a step size of 1 cm. The lookup table contained all the simulated radar signals within this parameter space. During inversion, these pre-calculated signals were used to compute the full objective function, allowing a fast, robust, and exhaustive search for the best-fitting solution. Regarding data filtering, the top 5 % of data points with the highest objective function values, indicating poorer fits between the model and observations, were excluded.

Then, the relative dielectric permittivity (ε_r) was converted into soil volumetric water content (*VWC*, cm^3/cm^3) using a site-specific calibration (Equation (1)). This was necessary because common calibration equations do not apply to peat soils (Kellner and Lundin, 2001), and ensures improved *VWC* estimation. The calibration was performed using Teros12 sensors (Meter Group, München, Germany) by rewetting several bulk peat samples from the study site, following the manufacturer's recommendations. Three bulk peat replicates were used, yielding 60 paired measurements of ε_r and *VWC*, covering a *VWC* range from 0.03 to 0.71. To include higher moisture conditions data, 18 additional points were added, corresponding to the laboratory-determined *VWC* at saturation aligned with the highest ε_r values recorded by the Teros12 sensors installed in the field. The resulting calibration curve was a 6th-order polynomial, with an R^2 of 0.99. This equation closely resembles that of Pepin et al. (1992), a widely used calibration for peat soils, showing a RMSE of 0.04 and a correlation of 0.99 between *VWC* modelled by Equation (1) and by Pepin et al. (1992). It should be noted that the use of a single calibration equation has limitations in peatlands, which are highly heterogeneous environments.

$$\mathrm{VWC} = -4.18\times10^{-11}\epsilon_r^6 + 1.17\times10^{-8}\epsilon_r^5 - 1.31\times10^{-6}\epsilon_r^4 + 7.46\times10^{-5}\epsilon_r^3 - 2.38\times10^{-3}\epsilon_r^2 + 5.15\times10^{-2}\epsilon_r - 3.25\times10^{-2} \quad \text{Equation 1}$$

2.3. On ground water content measurements

2.3.1. Temporal measurements (Teros12 probes)

To measure the temporal evolution of soil moisture using ground-based probes and to compare it with GPR measurements, Teros12 sensors (Meter Group, München, Germany) were used. These sensors use capacitance/frequency-domain technology, where charge time is proportional to substrate moisture. They were installed at five different topographic positions, with two replicates per position located 5 m apart

Table 1
Dates of the GPR measurements conducted from May 2023 to September 2024. Measurements were taken approximately once per month, increasing to twice per month during the summer due to higher moisture variability. No data were collected in June 2023 due to drone issues, and in December 2023 and January 2024 due to snow cover interfering with GPR measurements. [t] indicates dates when surface temperature data were also retrieved, and [m] indicates when multispectral data were also retrieved, both by Li et al. (2025).

Season	Spring 2023	Summer 2023	Autumn 2023	Winter 2023–2024	Spring 2024	Summer 2024
Measurement dates	16 May [t,m]	4 Jul. [t] 19 Jul. [t,m] 7 Aug. [t,m] 6 Sep. [t] 18 Sep.	4 Oct. 16 Oct. [m] 6 Nov.	2 Feb. [t,m] 13 Mar. [t,m]	25 Apr. 13 May [t,m] 12 Jun. [t,m]	1 Jul. 9 Jul. [t,m] 30 Jul. 13 Aug. 16 Sep.

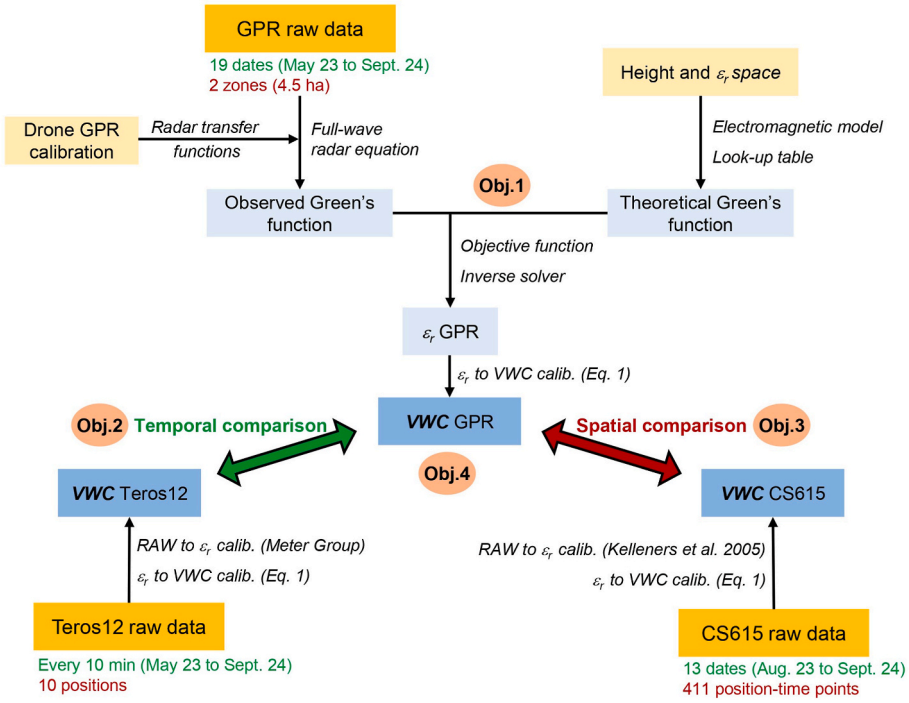

Fig. 3. Methodological flowchart of this study. The upper section of the workflow illustrates the full-wave radar data processing framework applied to the GPR data. The lower section shows the comparison between the GPR-derived *VWC* and on-ground probes measurements. The specific objectives (Obj. 1 to 4) are indicated at their corresponding stages in the workflow.

(Fig. 1). At each of these 10 positions, one sensor was placed at a depth of 10 cm and another at 30 cm. For comparison with GPR-derived *VWC*, the mean of the Teros12 readings at 10 and 30 cm depth was primarily considered, as this best approximates the 0–35 cm soil layer influencing the GPR measurements. It is worth noting that only 4 of the 10 sensor positions (the two from LS3 and the two from LS4) are located within the GPR measurement area (Fig. 1). All Teros12 sensors, except for the one located at 30 cm depth at LS2, were installed within the peat layer. The raw measurements from the Teros12 sensors installed in peat were converted to *VWC* using Equation (1), a site-specific calibration developed following the manufacturer's recommendations for optimal accuracy. The raw measurements from the Teros12 sensor installed in mineral soil were converted to *VWC* using Equation (2), the manufacturer-recommended calibration for mineral soils. These sensors monitored *VWC* with a 10 min interval from May 2023 to September 2024. For comparison with GPR-derived moisture, the Teros12 *VWC* was averaged on the day of the GPR measurements between 09:00 and 16:00, corresponding to the measurement period. This averaging was justified because *VWC* remained stable during these intervals (with a mean amplitude of *VWC* variation of 0.2 %), partly due to the absence of rainfall.

$$\mathrm{VWC} = 3.879 \times 10^{-4} \times RAW_{Teros12\ measurements} - 0.696 \qquad \text{Equation 2}$$

2.3.2. Spatial measurements (CS615 probe)

To better evaluate the spatial patterns of soil moisture using ground-based probes and to compare it with GPR measurements, a CS615 probe (Campbell Scientific, Logan, United States) was used. This portable water content reflectometer derives moisture information from the effect of changing dielectric permittivity on electromagnetic waves propagating along a waveguide (two steel rods of 30 cm long). The measurements were first converted to dielectric permittivity using the method of Kelleners et al. (2005), and then to *VWC* using Equation (1). On 13 different dates, measurements (ranging from 21 to 50 per date, with a mean of 32) were collected and dispersed across the two zones of interest. Each measurement involved measuring the *VWC* of the top 30 cm of the soil at three to four different locations within a 1 m^2 area (providing information about moisture variations at the decimeter scale), and then averaging these measurements. The locations of these measurements were recorded with a differential GPS, providing precision between 0.1 and 2 m depending on network conditions. In total, 411 measurements were collected between August 2023 and September 2024. The measurements were collected on the same day as the GPR ones, usually between 1 and 5 h afterward. No rainfall occurred during this time lapse, reducing the likelihood of important moisture changes. It is worth noting that CS615 measurements were not collected directly beneath the drone flight lines; instead, kriging interpolation was used to co-locate soil moisture estimates from the probe and GPR data, introducing corresponding uncertainties along with positioning error from the non-differential GPS used on the drone-borne GPR. The resulting spatial mismatch is at the meter scale.

2.3.3. Comparison between on-ground probes

A comparison between the two types of on-ground moisture probes used in this study was carried out based on data collected on seven different dates at four positions (LS3A, LS3B, LS4A, and LS4B). For the Teros12 probes, the mean *VWC* over a 1-h window before and after the CS615 measurements was used. For the CS615, three *VWC* measurements were collected within 1 m^2 around each Teros12 sensor. The two probes showed an acceptable correlation of 0.56 when comparing CS615

Table 2
Comparison between on-ground moisture probes: correlation between *VWC* derived from CS615 and Teros12 sensors, with different depths considered for Teros12 ($n = 28$). Significance levels are indicated as ** for p-value <0.01.

		Spearman correlation	R^2	RMSE
Depth of the Teros12 sensors	**10 cm**	0.58 **	0.33	0.11
	30 cm	0.09	0.01	0.15
	Mean 10 and 30 cm	0.56 **	0.30	0.12

data with the average of Teros12 readings at 10 and 30 cm depths (Table 2). The CS615-derived *VWC* was more closely related to the Teros12-derived *VWC* at 10 cm depth, consistent with its sensor length. The Teros12 systematically reported higher *VWC* values than the CS615. These differences arise from the different operating principles of the two probes, their different volumes and depths of measurement, the high spatial heterogeneity of moisture, and possible measurement errors. This suggests that, in peatlands, on-ground *VWC* sensors exhibit a certain degree of variability and should not be considered as absolute references. In conclusion, the objective of this study is to compare general temporal and spatial trends between GPR and on-ground methods, rather than to expect perfect agreement between them.

2.4. Water table depth data

Water table depth was monitored at the same five topographic positions as the Teros12 sensors (Fig. 1). Levelogger 5 pressure sensors (Solinst, Georgetown, Canada) were installed in PVC pipes to measure pressure, which was then used to infer water table depth. These sensors record measurements every 10 min from May 2023 to October 2024. Water table depth data were used to qualitatively compare its temporal evolution with GPR- and ground-probe- derived moisture. No further analyses were performed, as this study focuses on the link between GPR and soil moisture directly, and because the relationship between water table depth and soil moisture has already been examined in previous studies (e. g., Price, 1997).

2.5. Weather data

Weather data were acquired from the Mont-Rigi weather station, operated by the Royal Meteorological Institute of Belgium, located 2 km from the study site. Daily total precipitation was used. Potential evapotranspiration data, calculated using the Penman-Monteith daily equation based on the weather station data, were also used. Weather data were used solely for a qualitative comparison of their temporal evolution with the GPR-derived moisture. Further analysis in beyond the scope of this study and has already been reported in previous works (e. g., Bechtold et al., 2018).

2.6. Data analyses

2.6.1. Kriged maps of GPR-derived VWC

All data analyses in this study were conducted in RStudio (Posit, Massachusetts, United States) using R version 4.2.2. The GPR measurements, which provide point measurements of *VWC* but with a footprint representative of a larger area, were initially kriged to create continuous maps of root-zone moisture for the two different zones. First, the kriging grid was set up around the measurement zone with a buffer and with a grid resolution of 5 m. This resolution was chosen to match the 5 m GPS uncertainty, the 4–5 m^2 footprint of the drone-borne GPR system, and the 10 m spacing between adjacent measurement lines. Next, semivariograms were computed using the *fit.semivariogram* function from the *gstat* package (version 2.1.0) with a cutoff of 50 m and a width of 1 m. The model fitted to the data was an *Exclass* model, combining the *Exponential class* with the *Stable model*, with unweighted points. This combination is similar to the exponential model with a nugget usually used in moisture analysis studies (Brocca et al., 2007). This combination of model and fit method was chosen because it yielded the lowest mean absolute error. Nuggets ranged from 0 to 0.03 m (mean 0 m), sills ranged from 0.04 to 0.10 (mean 0.07), and ranges varied from 0.5 to 96 m (mean 5.2 m), the semivariograms are presented in Fig. 4. Finally, the data were kriged using the *krige* function of the *gstat* package based on the optimized semivariograms. The kriging standard deviation, representing the expected uncertainty of predicted *VWC* at each grid point, ranged from 0.11 to 0.31, with per-map median values between 0.19 and 0.29 (mean 0.25). This high uncertainty is related to the high micro-variability in *VWC* derived from the GPR measurements. Further details on uncertainties associated with kriging of GPR-derived moisture are presented in Minet et al. (2012).

2.6.2. Comparison of GPR-derived and on-ground VWC measurements (spatial and temporal analyses)

First, the kriged GPR data were compared temporally with the Teros12 data to evaluate the capability of GPR to track temporal changes in root-zone moisture. This comparison was possible because the Teros12 sensors were permanently installed and continuously recorded the evolution of soil moisture over time. Spearman correlations, associated p-values, and RMSE between the two datasets were calculated for both overall temporal moisture changes (mean moisture values for the entire zone from GPR and for the 10 Teros12 positions) and local temporal moisture changes (at the LS3 and LS4 topographic positions, Fig. 1). Spearman correlations were used because of the non-normal distribution of the *VWC* data. First, correlations were calculated using the mean of Teros12 readings at 10 and 30 cm depth, corresponding to the GPR's effective sensing depth, while additional analyses where performed afterward for each depth separately. For the local comparison, GPR derived *VWC* was averaged over different radii of influence, ranging from 5 to 20 m.

Second, the kriged GPR data were compared spatially with the CS615 data to evaluate the capability of GPR to map spatial variations in root-zone moisture. This comparison was possible because multiple discrete CS615 measurements were realized, allowing to gain information dispersed across the entire GPR measurement zone. Spearman correlation, the associated p-values, and the RMSE between the two datasets were calculated.

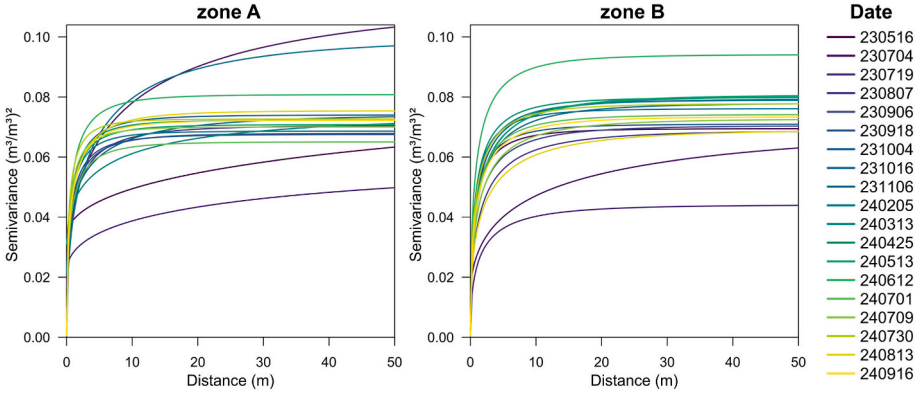

Fig. 4. Semivariograms of the kriging models of *VWC* derived from GPR measurements, shown for the two study zones across the 19 different dates (in the yymmdd format).

2.6.3. Spatial clustering of GPR-derived VWC

A clustering analysis was performed to identify zones of similar moisture over time. The clustering area was selected based on zones sensed at least 50 % of the time by the GPR. The input data for clustering included all 19 kriged *VWC* maps derived from GPR measurements. Missing values were replaced by the mean *VWC* of the other dates at the same location. First, the number of clusters was optimized to three, as increasing beyond three resulted in only a marginal reduction in the within-cluster sum of squares. Second, the clustering was conducted using the K-means algorithm (*kmeans* function from the *stats* package, version 4.2.2), which groups data into clusters by iteratively assigning points to the nearest centroid and updating the centroids. No constraint was set on the minimum number of adjacent pixels within a cluster, this could be considered for further studies depending on the targeted applications. Because this clustering is based on 19 maps, it highlights large-scale, consistent moisture patterns that may not be visible in individual moisture maps, capturing both the average moisture levels and the amplitude of moisture variations.

2.6.4. Comparison of GPR-derived VWC with site characteristics

The moisture clusters were compared with various available characteristics of the study site. First, vegetation composition data at a resolution of 0.45 m were used in this analysis. These data were provided by Li et al. (2024), who used a Random Forest model for land cover classification based on multiple vegetation indices derived from multispectral and LiDAR imagery for the 12 main dominant vegetation types of the study site. Statistical differences in vegetation cover between clusters were assessed using a Chi-square test (*chisq.test* function from the *stats* package). Second, the clusters were compared with peat depth data from Li et al. (2024), aggregated at a resolution of 5 m to match the resolution of the clusters. Third and fourth, the clusters were compared with slope and Topographic Wetness Index (TWI; Beven and Kirkby, 1979) as determined by Li et al. (2024) at a resolution of 4.8 m. Fifth, they were compared with the mean NDWI across 10 different dates (presented in Table 1) retrieved by Li et al. (2025) using a Matrice 300 RTK drone (DJI, Shenzhen, China) and a MicaSense RedEdge-M camera (MicaSense, Seattle, United States) aggregated at a resolution of 5 m. Sixth, the clusters were compared with the mean surface temperature across 9 different dates (presented in Table 1) retrieved by Li et al. (2025) using a Matrice 300 RTK drone and a ThermalCapture camera (TeAx Technology, Wilnsdorf, Germany) aggregated at a resolution of 5 m. For peat depth, slope, TWI, NDWI, and surface temperature, the Kruskal-Wallis test was used to evaluate statistical differences among the three moisture clusters, followed by a Dunn posthoc test with Bonferroni correction for pairwise comparisons between clusters (*kruskal.test* and *dunn.*test functions from the *stats* package).

In addition, the continuous site characteristics were compared with the mean *VWC* derived from the GPR measurements across the 19 dates. The continuous variables considered were peat depth, slope, TWI, mean surface temperature, and mean NDWI. Spearman correlations and associated p-value were calculated to assess these relationships.

3. Results and discussion

3.1. Drone-borne GPR derived root-zone moisture maps

Moisture maps (after kriging) of the two zones of interest are presented for nine of the nineteen different dates between May 2023 and August 2024 in Fig. 5. The *VWC* ranges from 0.1 to 1, with most values falling between 0.4 and 0.7. These relatively high moisture contents are consistent with peat properties, particularly its high porosity. Zone A consistently shows higher moisture content than zone B (Figs. 5 and 6a). This is due to zone A's flatter topography, allowing more water accumulation, and to the higher drain density in zone B.

Moisture exhibits substantial micro-variability (at a decimeter to meter scale), with highly variable moisture contents in close proximity. This variability in the measurements may partly result from small fluctuations in the incidence angle. However, Wu and Lambot (2022a) reported absolute errors in permittivity estimation of up to 3 for an incidence angle of 10° and up to 8 for an incidence angle of 30°. Yet, in this study, we used a dipole antenna, which is much less sensitive to incidence angle changes than the horn antenna used by Wu and Lambot (2022a), suggesting that the associated error is smaller. Moreover, the slow flight speed likely limits variations in the incidence angle. Thus, the measurement variability can primarily be attributed to inherent small-scale moisture variations. Additionally, the GPR measurements are also influenced to a lesser extent by changes in microtopography and vegetation heterogeneity, both of which affect moisture distribution and surface ponding. It is important to note that some of these small-scale variations in root-zone moisture are averaged out by the large GPR footprint (approximatively 4–5 m^2). These small-scale moisture variations in peatlands can be linked to variations in organic matter content, saturated hydraulic conductivity (Wang et al., 2021), bulk density and the changes in vegetation types. Next, some of the micro-variability is linked to the positioning of the measurements, as some directional patterns may appear due to the flight direction, as visible in Fig. 5e. An improvement in this regard could be achieved by mapping the field with drone surveys conducted in two directions and using a smaller spacing between flight lines. The large micro-variability in moisture means that the ranges of the semivariograms used for kriging are very small, with the median being 1.1 m, which is among the lowest values reported in the literature for soil moisture (Western and Blöschl, 1999). There is no nugget effect for 31 of the 38 grids, indicating that the measurements are consistent at very small scales. The consistency of moisture micro-variability was not investigated in this study due to the averaging effect of the large GPR footprint and the lack of accuracy of the non-differential GPS used, but it would represent an interesting direction for future studies.

Macro-variability (tens of meters) in moisture patterns also appears (Fig. 5). Some of this variability is consistent across the different dates. For example, two wetter zones are observed: one in the north-central region of zone A and another in the south-central region of zone B. Petrone et al. (2004) reported a persistence of 60 % in spatial patterns over time in a peatland, whereas in our study some small patterns are similarly persistent. As observed by Rosenbaum et al. (2012), the data appeared more dispersed under intermediate moisture conditions. In drier conditions, the moisture patterns are smoother. Zone B shows a stronger spatial organization, along with a higher range, partially attributed to a steeper slope (Brocca et al., 2007).

3.2. Temporal monitoring of peatland moisture using drone-borne GPR

3.2.1. Peatland moisture evolution during the monitoring period

The GPR was used for almost one and a half years to monitor the moisture in the top 35 cm of peat. In May 2023, the site-mean GPR-derived moisture was 0.61, indicating moderately wet conditions (Fig. 6a), while Teros12 sensors indicated near saturated conditions (Fig. 6d). By July 19, GPR-derived moisture dropped to a mean of 0.47, which is the lowest *VWC* of the entire observation period. Water table heights (Fig. 6c) and Teros12-derived *VWC* also showed a decrease lasting to the end of July, due to early summer dry conditions (Fig. 6b). On August 7, GPR-derived *VWC* rose sharply to 0.54. This was caused by heavy rainfall, and is aligned with the rising water table and Teros12 VWC measurements. Afterward, GPR-derived moisture continued to rise gradually until February 2024, when it reached its maximum at 0.67. This is coherent with the sustained high rainfall during autumn and winter 2024. During this period, water tables also rose progressively, while the Teros12 sensors were already showing saturated conditions most of the time. The GPR-derived *VWC* remained relatively stable until May 2024. A slight gradual decline was then observed from May to July, and by August 13, the minimum GPR-derived *VWC* for summer 2024 was observed at 0.58, corresponding to a drier period and a drop in

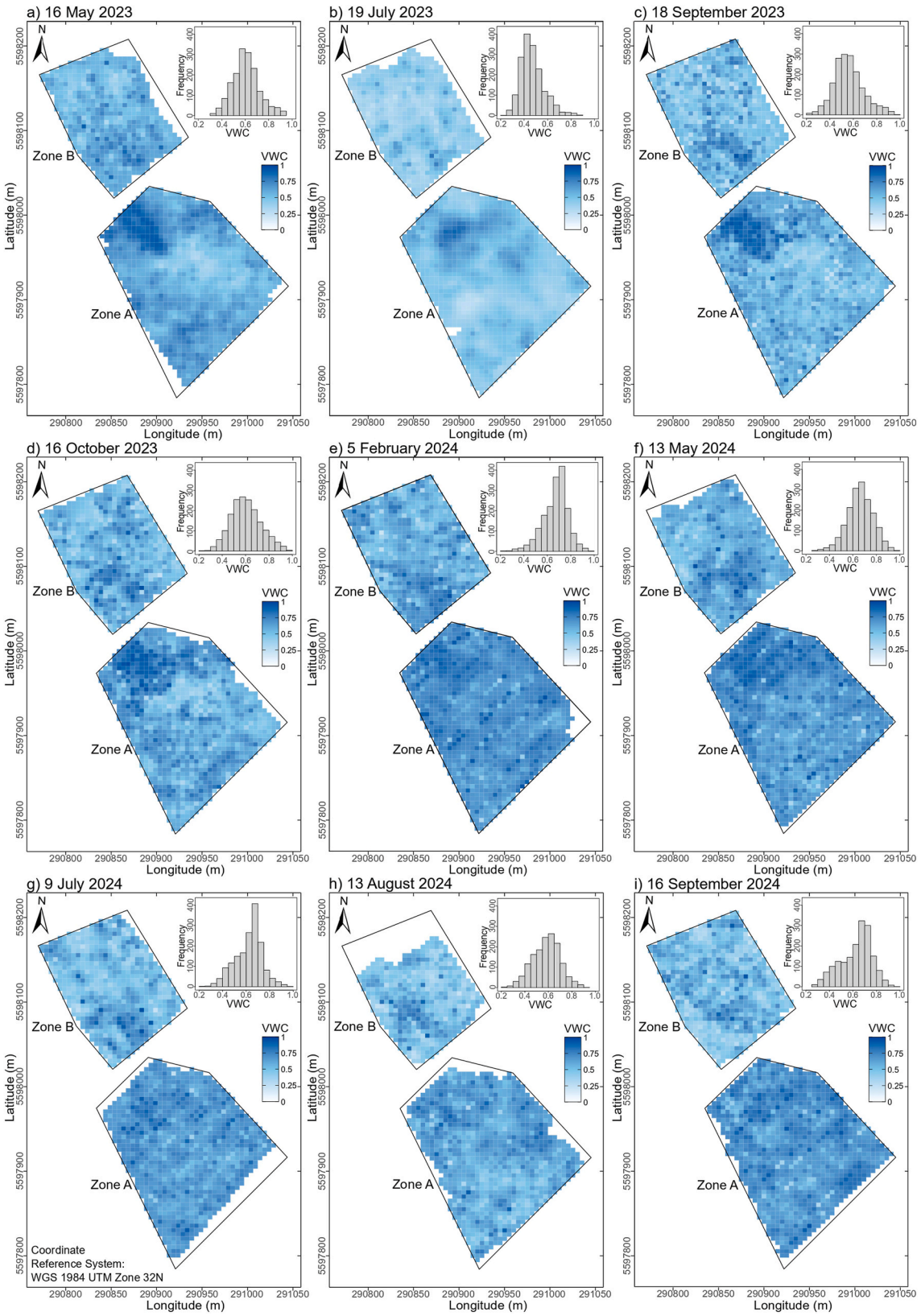

Fig. 5. GPR-derived root-zone moisture maps after kriging at a resolution of 5 m for nine different dates. The histograms of the *VWC* in each pixel are also presented for each date. (a) May 16, 2023. (b) July 19, 2023. (c) September 18, 2023. (d) October 16, 2023. (e) February 5, 2024. (f) May 13, 2024. (g) July 9, 2024. (h) August 13, 2024. (i) September 16, 2024.

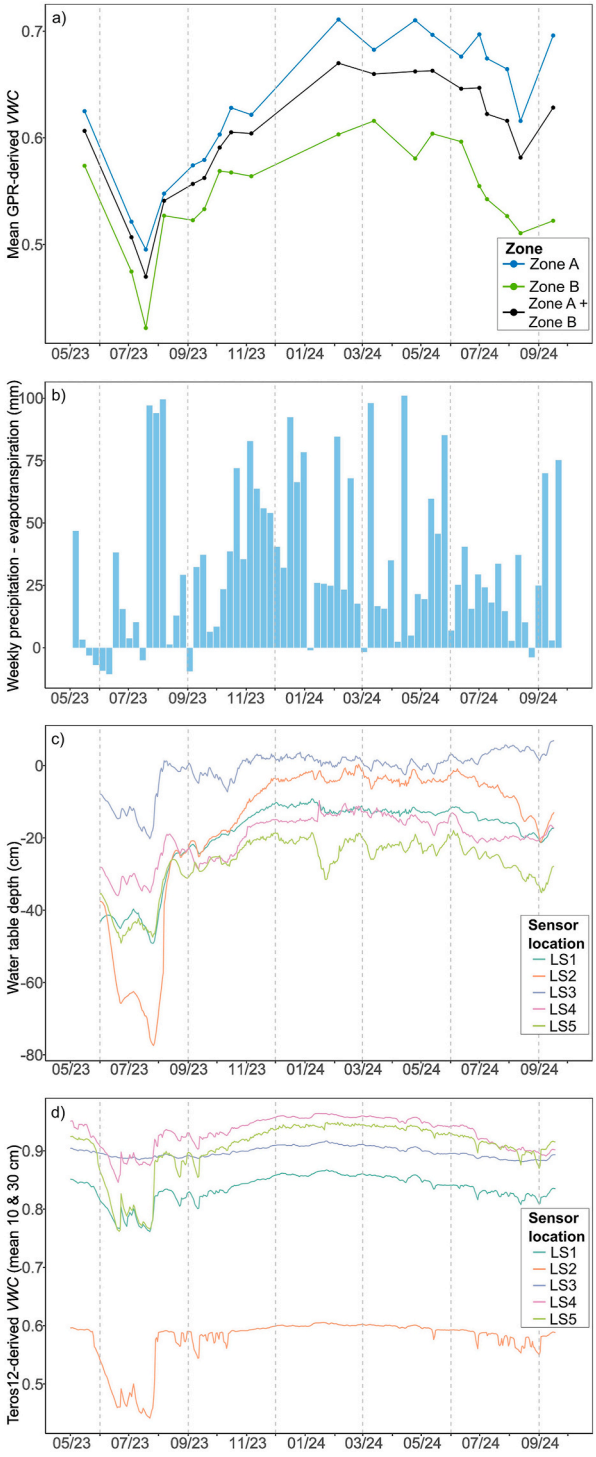

Fig. 6. Evolution of moisture-related parameters over time between May 2023 and September 2024. (a) Mean of the GPR-derived *VWC* after kriging in the zones A and B, as well as the overall mean. (b) Weekly precipitation minus potential evapotranspiration. (c) Water table depth at the five topographic positions. (d) Average *VWC* measured by Teros12 sensors at 10 and 30 cm depths across two replicates at the five positions.

Teros12 sensor measurements. Subsequently, GPR measurements in September showed an increase in *VWC* to 0.63, consistent with water table heights and Teros12 measurements. In summary, the GPR-derived *VWC* exhibited clear seasonal behavior consistent with weather conditions and water table levels (Bourgault et al., 2019). Our approach successfully captured two contrasting summer conditions: a drier summer in 2023 and a wetter one in 2024.

3.2.2. Comparison between GPR- and ground-probe-derived temporal VWC

As a first step to obtain a general overview of seasonal moisture changes, GPR-derived *VWC* was compared with in situ measurements from the Teros12 sensors. The overall area comparison used the mean of GPR measurements across the two zones and the mean of the 10 Teros12 sensors locations, considered as representative of the moisture variations across the study area. The mean of their readings at 10 and 30 cm depth is first considered. The Spearman correlation between the two datasets is 0.71 (p-value <0.001), and the R^2 of the linear model is 0.74 (Fig. 7a). This indicates a good overall correspondence, that can be explained by the fact that both variables are influenced by the same factors, mainly climatic conditions. This relationship can also be examined separately for the 10 and 30 cm depths measured by the Teros12 sensors (Table 3). At the overall scale, the 30 cm depth shows higher correlation, because it is less affected by local and short-term *VWC* variations. It should be noted that the *VWC* derived from GPR (ranging from 0.47 to 0.67) is lower than the one recorded by the Teros12 sensors (ranging from 0.75 to 0.86). This difference is due to the fact that the two methods do not measure exactly the same property: the Teros12 measures *VWC* directly in the soil at specific depths, while the GPR method integrates a larger volume and is influenced by surface roughness and vegetation when it is dense (likely including the 5–10 cm of organic debris and vegetation above the soil surface), resulting in lower moisture estimates.

As moisture is highly heterogeneous in peatlands, it is primordial to evaluate the capability of GPR to monitor moisture changes locally. To this aim, a more localized comparison can be made between GPR and Teros12 at specific points, here LS3 in zone A and LS4 in zone B, where measurements overlap (Fig. 1). For the Teros12 data, the mean of the two replicates located 5 m apart was used, while for GPR, the average *VWC* of pixels within a 20 m radius around the centers of LS3 and LS4 was first considered. The 20 m radius was chosen to include a sufficient number of pixels to minimize the potential impact of errors in individual pixels on the result. Moreover, the general moisture conditions within this radius appeared to be broadly comparable. At LS3, the Spearman correlation is 0.22 (non-significant) and the R^2 of the linear model is 0.01 (Fig. 7b). In contrast, at LS4, the Spearman correlation is 0.71 (p-value <0.001) and the R^2 of the linear model is 0.51 (Fig. 7c), reflecting a much stronger correlation. Then, the same analysis was repeated for other radii (5, 10 and 15 m) around the centers of LS3 and LS4 to verify the representativeness of these results (Table 4). At LS3, correlations remained low and non-significant across all radii. At LS4, correlations were higher and significant, with better performance at larger radii, probably because the larger area is smoothing out smaller-scale *VWC* variability. When examining the 10 and 30 cm depths separately for the Teros12 sensors, they showed comparable results at LS3 and higher correlations at 10 cm for LS4. The general weaker performance at LS3 may be explained by the fact that this location remains saturated throughout the year (Fig. 6d) and is therefore showing little moisture variability (maximum *VWC* difference of 0.03 in Teros12 measurements), whereas LS4 exhibits more variability in moisture (maximum *VWC* difference of 0.08).

3.2.3. Comparison of GPR temporal moisture monitoring with other studies

The drone-borne GPR method presented in this study successfully captures the overall moisture changes over a period of more than a year, with sufficient sensitivity to capture different summer period conditions. The overall temporal Spearman correlation is 0.71, while local analyses show correlations of 0.22 (in a saturated area) and 0.71 (in an unsaturated area). These values can be compared to those from other studies, particularly satellite-based studies estimating water table depth variations over time (because there is a lack of studies using satellite data to predict moisture directly in peatlands). However, soil moisture and water table depth evolution are closely linked, providing general

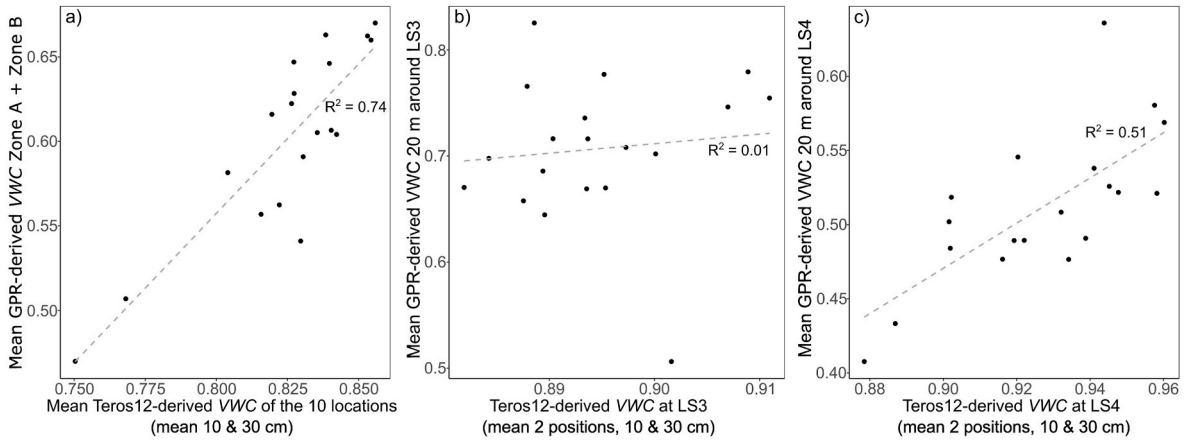

Fig. 7. Scatterplots comparing GPR-derived moisture and Teros12 moisture (mean of 10 and 30 cm depths) over time. (a) Overall study site: comparison between the mean GPR *VWC* across the entire area and the mean Teros12 VWC from the 10 points of interest. (b) LS3 position: comparison between the mean GPR-derived *VWC* within a 20 m zone around LS3 and the mean Teros12 VWC from the two replicates at LS3. (c) LS4 position: comparison between the mean GPR-derived *VWC* within a 20 m zone around LS4 and the mean Teros12 VWC from the two replicates at LS4.

Table 3
Summary of the overall temporal comparison between GPR-derived *VWC* and Teros12 sensors *VWC*. Spearman's correlations, R^2 of the linear model, and RMSE are reported. Results are shown for different Teros12 measurement depths. Significance levels are indicated as ** for p-value <0.01, and *** for p-value <0.001.

		Spearman correlation	R^2	RMSE
Depth of the Teros12 sensors	**10 cm**	0.70 **	0.71	0.22
	30 cm	0.82 ***	0.78	0.23
	Mean 10 and 30 cm	0.71 ***	0.74	0.23

insights into peatland moisture dynamics. The overall correlation and that for the unsaturated area lie at the higher end of those reported in the literature for satellite-based methods. Indeed, studies using optical indices report mean correlations of 0.57 for NDVI, 0.77 for NDWI (Linkevičienė et al., 2023), and 0.6 for OPTRAM (Burdun et al., 2023). Satellite-based radar approaches show mean correlations ranging from 0.38 to 0.77 (Asmuβ et al., 2019; Bechtold et al., 2018; Lees et al., 2021). This positions drone-borne GPR among the most accurate current approaches for remotely sensed peatland moisture monitoring. Furthermore, unlike many studies concentrating on water table dynamics, our approach directly targets peat moisture content which is more variable but more directly linked to vegetation and microbial activity (Kechavarzi et al., 2010; Price, 1997).

Regarding the limitations of the presented methods, both optical and radar satellite techniques are sensitive to the presence of dense vegetation, which reduces their effectiveness. In contrast, our method has a reduced sensitivity to vegetation, owing to the relatively long wavelengths (2.4–2.9 m) involved in this frequency range. The satellite methods are also offering coarser resolution than the drone-borne GPR but provide data over larger areas. Furthermore, optical and radar satellite methods show limited success in the case of deep water tables (>60 cm for radar according to Asmuβ et al., 2019). Although we did not assess very deep water tables in our study (maximum of 40 cm recorded by the sensors at a local scale), our method measures moisture content directly rather than water table depth, which could support its effectiveness at varying water table depths. Radar satellite methods are also less effective for shallow water tables (<20 cm) due to limited variations in water table depth over time. This limitation was also observed in our study, since our method shows limitation at the LS3 position. In fact, in wet areas, the soil reflection coefficient becomes less sensitive to changes in permittivity (and related *VWC*) and the signal-to-noise ratio increases, which limits the detection of small moisture changes by the GPR. Nevertheless, in unsaturated areas (LS4 position), our technique demonstrated the ability to detect small temporal moisture changes (below 5 % in *VWC*), whereas other studies have not achieved this level of precision (Jacome et al., 2013). To conclude, our method is one of the few that uses drone-based sensors to monitor peatland moisture dynamics over time and could complement satellite-based remote sensing approaches (Ghazaryan et al., 2024). However, further testing across diverse peatland states and water table depth conditions is necessary to establish its robustness across sites.

3.3. Mapping spatial variability of peatland moisture using drone-borne GPR

3.3.1. Comparison between GPR- and ground-probe-derived spatial VWC

The CS615 probe was used to spatially compare on-ground moisture measurements with those from the GPR. The Spearman correlation between the CS615 and the GPR-derived moisture varied from −0.28 to 0.61 across the dates, with a median of 0.28. The correlation thus fluctuated over time and was lower when more measurements were taken on the same date, indicating greater dispersion in the relationship.

Table 4
Summary of the local temporal comparison between GPR-derived *VWC* and Teros12 sensor data at two specific locations (LS3 and LS4, Fig. 1). Spearman's correlation, R^2 of the linear model, and RMSE are reported. Results are shown for four radii around the LS3 and LS4 centers used for averaging GPR derived *VWC*. Significance levels are indicated as * for p-value <0.05, ** for p-value <0.01, and *** for p-value <0.001.

		LS3 location			LS4 location		
		Spearman correlation	R^2	RMSE	Spearman correlation	R^2	RMSE
Radius for GPR-derived *VWC* averaging	**5 m**	0.18	0.12	0.17	0.62 *	0.43	0.45
	10 m	0.28	0.09	0.17	0.52 *	0.48	0.43
	15 m	0.28	0.03	0.19	0.70 **	0.47	0.42
	20 m	0.22	0.01	0.20	0.71 ***	0.51	0.42

The overall Spearman correlation across all the dates is 0.23 (p-value <0.001), the RMSE is 0.16, and the R^2 is 0.05, which is low (Fig. 8). First, it is important to note that the micro-variability in both types of measurement is high. For the CS615 probe, the standard deviations of the 3 to 4 measurements within 1 m^2 ranged from 0 to 0.26 (*VWC*), with a mean of 0.06. For GPR, the standard deviation of kriging was high and ranged from 0.12 to 0.31 (*VWC*), with a mean of 0.25. It is worth noting that the standard deviation decreases as *VWC* increases, which is logical because less variability in moisture is observed in wetter areas. This very high micro-variability is well-known in peatlands for vegetation (Räsänen and Virtanen, 2019), microtopography (Petrone et al., 2004), and hydraulic properties (Wang et al., 2021), all of which are related to moisture. This micro-variability is thus one of the main factors explaining the limited correlation obtained. Another cause is the spatial mismatch: the two measurements are not taken at exactly the same location, with CS615 measurements being compared to kriged GPR ones. Furthermore, the two methods have different volumes of influence (about 0.007 m^3 for the CS615 and 1.6 m^3 for the GPR, resulting in an approximately 225-fold higher volume for the GPR). Additionally, GPR measurements at high moisture content, which is the case in peatlands, have greater uncertainty due to reduced sensitivity of the reflection coefficient.

3.3.2. *Comparison of GPR spatial moisture mapping with other studies*

Our results can be compared with those from other studies regarding spatial variations in peatland moisture. Satellite-based studies that combine optical and radar sensors to predict water table depth or moisture content in peatlands obtained R^2 values of 0.71 and 0.93 (Isoaho et al., 2024; Klinke et al., 2018). Drone-based studies using optical and thermal data reported average R^2 values ranging from 0.38 to 0.73 for water table depth or soil moisture prediction (de Lima et al., 2022; Isoaho et al., 2023; Lendzioch et al., 2021; Wigmore et al., 2019). However, these approaches face limitations in areas with high spatial heterogeneity in vegetation, topography or hydrology and often fail to generalize across different sites or monitoring periods. Our method seems to be less successful in capturing accurate moisture content values

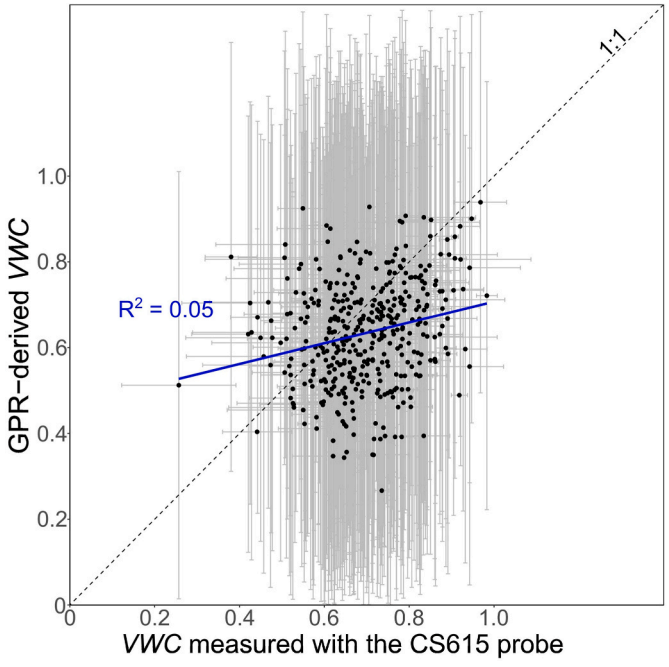

Fig. 8. Scatterplot showing *VWC* measured using the CS615 probe (3–4 measurements within 1 m^2, with the average and standard deviation presented), compared to *VWC* derived from GPR measurements after kriging, with the kriging standard deviation of the pixel also displayed.

across spatial scales when compared to on-ground probes. This is because direct validation through a precise spatial comparison was not possible due to GPS positioning errors of the drone and the effects of kriging interpolation. For a more accurate comparison, measurements would need to be collected at the same points, which could be achieved by using the drone-borne GPR to hover above specific locations where on-ground measurements are collected. Furthermore, spatial correlations between ground-based probes and remotely sensed moisture are generally lower than those observed for water table depth (Lendzioch et al., 2021). Despite these limitations, our results remain encouraging and are interesting because, unlike satellite methods, GPR provides direct information on the subsoil.

Several technical improvements could also be applied in future studies to further enhance our methodology. Improvements could include maintaining a more stable flight height to reduce potential errors (Pramudita et al., 2022) and minimizing the range of potential flight heights in the lookup table used in the inversion method, as well as keeping a constant speed to reduce the effects of changing incidence angle (Wu and Lambot, 2022a). Additionally, using a differential GPS, reducing the spacing between flight lines, and conducting bidirectional flights could improve spatial resolution. Another potential advancement includes accounting for vegetation effects (Pramudita et al., 2022). An additional improvement involves combining GPR data with relevant covariates and applying machine learning approaches. Finally, it would be worthwhile to test whether the inclusion of GPR data alongside more commonly used drone-based optical and thermal data could improve the prediction accuracy of peatland root-zone moisture patterns.

3.4. *Clustering analysis of spatial moisture patterns and comparison with site variables*

The clustering based on the 19 moisture maps generated a map of three distinct soil moisture classes across the study area (Fig. 9a). These three classes are relatively homogeneous in space and delineate clear moisture patterns that align well field observations, supporting the reliability of the resulting map, especially as it integrates data from multiple seasons. The high moisture content class is mainly located in the northern part of zone A and in the central-southern area of zone B. The low moisture content class occupies most of the rest of zone B, while the intermediate moisture content class covers most of the remaining areas of zone A. The GPR-derived volumetric water content differs significantly among the three classes (p-value <0.001), with average *VWC* calculated from the 19 dates of 0.52 ± 0.05 in the low moisture zone, 0.61 ± 0.08 in the intermediate moisture zone, and 0.70 ± 0.06 in the high moisture zone (Fig. 10a). Below, we explore whether these three classes of moisture content are linked to other key site characteristics.

First, vegetation composition differs among the three moisture classes (Fig. 9b). Specifically, the relative area occupied by each vegetation type shows significant differences for blueberry (*Vaccinium myrtillus*; p-value <0.001), purple moor grass (*Molinia caerulea*; p-value <0.05), and rush (*Juncus acutus*; p-value <0.01). Blueberry cover tends to increase as conditions become drier: it covers 11 % of the high moisture class and 37 % of the low moisture class (Fig. 10b). This is consistent with studies showing the expansion of blueberry in response to peatland drying (Bragazza, 2006; Bragazza et al., 2015). In contrast, rush, which tolerates waterlogged conditions (Bettink, 2009), is more present in the high moisture class (21 %) than in the low moisture class (5 %). *Molinia caerulea* is more prevalent in the high moisture class, despite its preference for moderately moist rather than saturated conditions (Gatis et al., 2016). *Molinia caerulea* is actually the dominant vegetation of the site, as it spreads quickly on peatlands that were partially exploited (Frankard, 2004). We hypothesize that its higher presence in the high moisture class is most likely due to the absence of blueberry, allowing it to occupy much of the remaining space. *Sphagnum* mosses, being good indicators of waterlogged areas (González et al.,

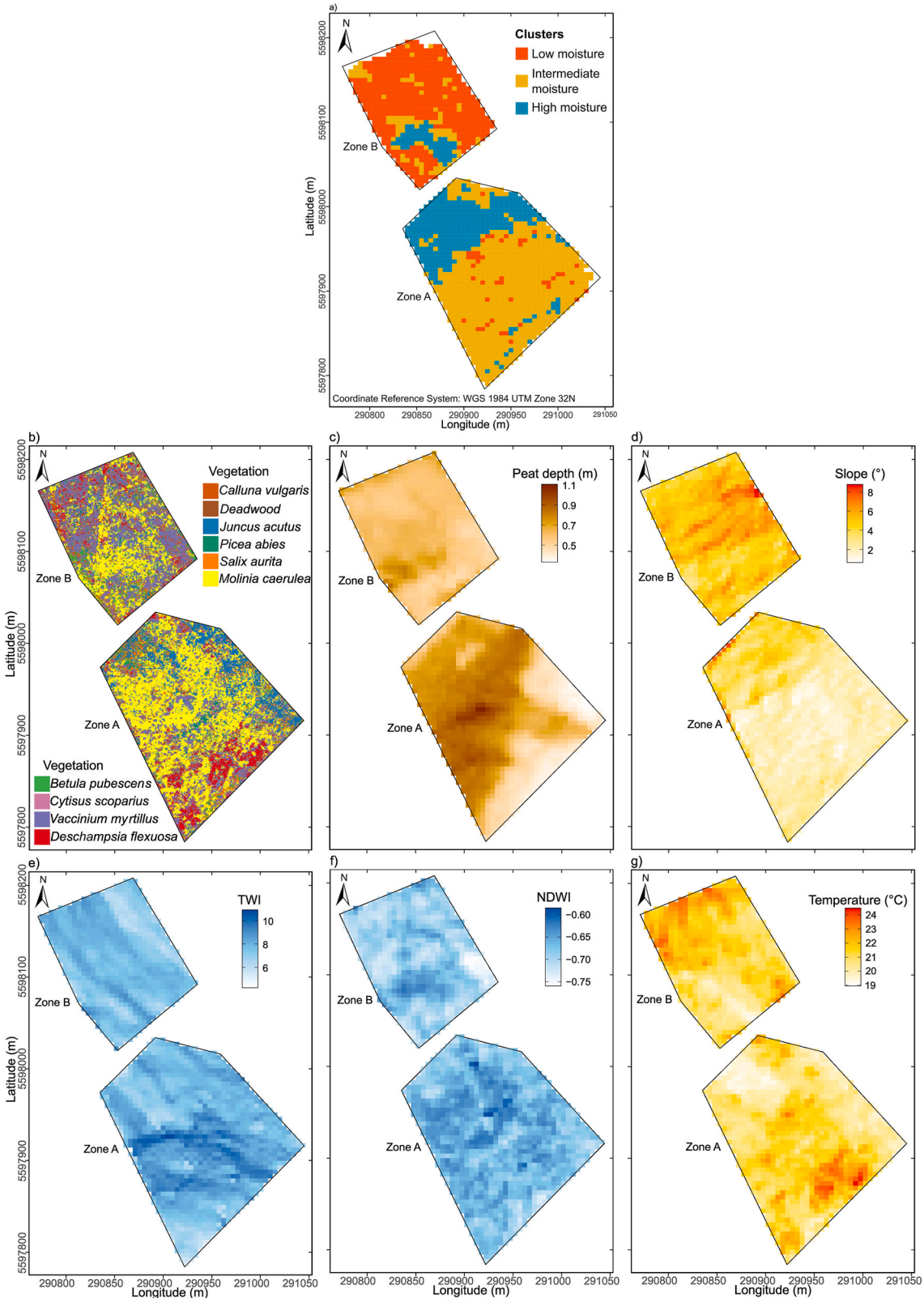

Fig. 9. Comparison between the three classes of soil moisture resulting from the K-means clustering and other variables of interest. (a) Map of the three soil moisture clusters. (b) Map of vegetation cover. (c) Map of peat depth. (d) Map of slope. (e) Map of the TWI. (f) Map of the mean NDWI across 9 dates. (g) Map of the mean surface temperature across 10 dates.

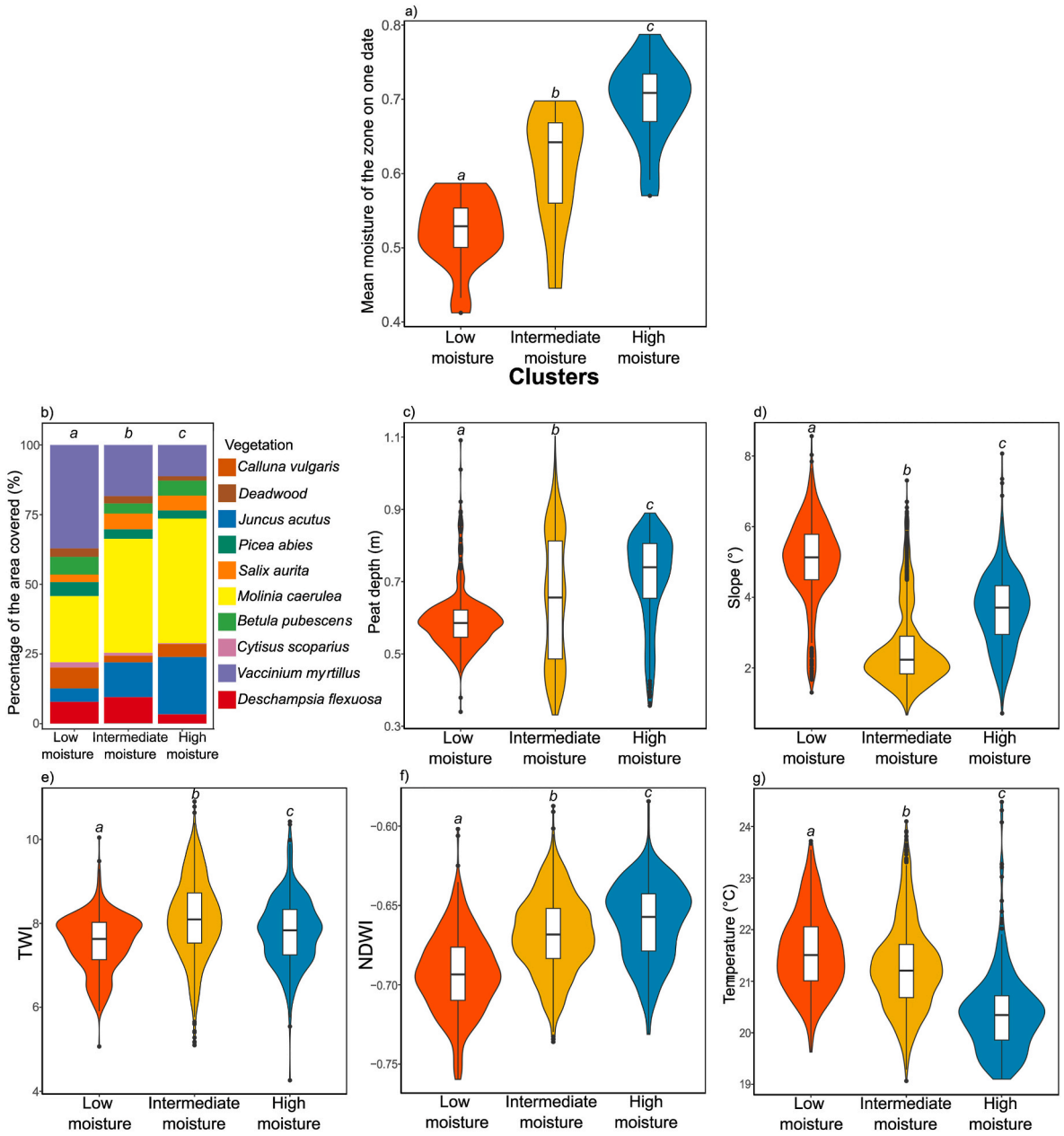

Fig. 10. Comparison between the three classes of soil moisture resulting from the K-means clustering and other variables of interest. The differences between the three clusters (pairwise comparison from the Dunn test) are indicated by different letters in the boxplots when significant (p-value <0.01). (a) Distribution of mean moisture on one date in the three soil moisture classes. (b) Percentage of area covered by each type of vegetation in the three clusters. (c) Peat depth distribution in the three clusters. (d) Slope distribution in the three clusters. (e) TWI distribution in the three clusters. (f) Mean NDWI distribution in the three clusters. (g) Mean surface temperature distribution in the three clusters.

2014), would be interesting to compare between the moisture classes. However, it is challenging to detect them on this site because they often grow below other vegetation, and, consequently, not accounted for in Li et al. (2024).

Second, regarding peat depth, distinct patterns are observed across the study site (Fig. 9c), with significant differences among the three moisture classes (p-value <0.001). The low moisture class has a relatively homogeneous thin peat layer, with a mean peat depth of 0.59 ± 0.08 m, which is the shallowest of the three classes (Fig. 10c). In contrast, the high moisture class is covered by deeper peat (mean peat depth of 0.71 ± 0.12 m). The intermediate moisture class displays considerable variability in peat depth (mean peat depth of 0.65 ± 0.18 m). The shallower peat in the south-eastern part of zone A corresponds to an area of silty soil (Henrion et al., 2024). The presence of deeper peat in the wetter areas is consistent with the fact that peat forms in water-saturated conditions (Holden, 2006). This observation is in line with other studies reporting strong links between the moisture status and peat depth (Ågren et al., 2022; Sun et al., 2023). Supporting this, the mean *VWC* measured over the 19 dates is positively and significantly correlated with peat depth (0.24; Table 5).

Third and fourth, the slope of the study site and the Topographic Wetness Index (TWI) show clear variations (p-value <0.001) associated with the three moisture classes (Fig. 9d and Fig. 9e). The low moisture class is located on the steepest slopes (mean of 5.0 ± 1.2°; Fig. 10d) and has the lowest TWI (mean of 7.5 ± 0.7; Fig. 10e). The intermediate moisture class occupies the lowest slopes (mean of 2.6 ± 1.2°) and has the highest TWI (mean of 8.1 ± 1.0). Finally, the high moisture class is found on moderately sloped areas (mean of 3.6 ± 1.1°) and shows an

Table 5
Spearman correlation between the mean GPR-derived *VWC* over the 19 measurement dates and continuous site characteristics. Significance levels are indicated as *** for p-value <0.001.

	Peat depth	Slope	TWI	Mean NDWI	Mean surface temperature
Mean GPR-derived *VWC*	0.24 ***	−0.30 ***	0.10 ***	0.42 ***	−0.48 ***

intermediate TWI (mean of 7.8 ± 0.8). The results for the low moisture class are as expected, corresponding to the steepest slopes and the lowest TWI (Ikkala et al., 2022). However, the topographic conditions of the intermediate moisture class, characterized here by the gentlest slopes and highest TWI, are more favorable to higher wetness than those of the high moisture class. This suggests an unexpected relationship between moisture and topography for these two classes. This inconsistency could be due to several factors: (i) moisture is influenced not only by general slope but also by microtopography (Petrone et al., 2004), which plays a significant role (de Lima et al., 2022) but is not captured at the scale used in this study (4.8 m resolution); (ii) the ability of the TWI to predict wetness is scale-dependent, making it less suitable for mapping small-scale variations of moisture in peatlands (Ågren et al., 2014; Hasan et al., 2012); (iii) the relationship between peatland moisture and TWI is not necessarily positive in flatter areas (Isoaho et al., 2023). A finer resolution comparison could be useful to investigate the links of topography with soil moisture. However, when considering the mean *VWC* across the 19 dates, it is significantly negatively correlated with slope (−0.30; Table 5) and positively correlated with TWI (0.10; Table 5), as expected.

Fifth, the moisture classes can be compared with NDWI, a multispectral index initially created to detect open water features (McFeeters, 1996), but also used to detect vegetation drought response (Gu et al., 2008). Higher NDWI values are thus considered to align with higher surface moisture. The NDWI patterns in zone B align closely with those of the moisture classes, with a low NDWI across most of the zone and a higher one in the central-southern area, while the pattern is less clear in zone A (Fig. 9f). The NDWI values are significantly linked (p-value <0.001) to the moisture classes, with a mean NDWI of −0.69 ± 0.02 for the low moisture class, a mean NDWI of −0.67 ± 0.02 for the intermediate moisture class, and a mean NDWI of −0.66 ± 0.02 for the high moisture class (Fig. 10f). It is worth noting that the correspondence between moisture and NDWI is not always straightforward in peatlands, as previous studies have found both positive (Isoaho et al., 2023; Lees et al., 2020) and negative (Linkevičienė et al., 2023; Zhang et al., 2014) correlations. In this study, NDWI seems particularly effective at delineating the low moisture class. Additionally, the correlation between mean *VWC* and mean NDWI over the study period is positive and significant (0.42; Table 5). A promising future approach could involve using NDWI derived from hyperspectral data, which has shown good results in peatlands, both in field (Meingast et al., 2014) and drone studies (Kalacska et al., 2018).

Sixth, the moisture classes can be compared with surface temperature data. It is well known that temperature can rise with water stress (Goetz, 1997), suggesting a link between surface temperature and soil moisture (Reiniger and Seguin, 1986). At our study site, the zones of low surface temperature closely resemble the high moisture class (Fig. 9g). The mean temperature for this class is 20.4 ± 0.8 °C, while it is 21.3 ± 0.9 °C for the intermediate moisture class, and 21.6 ± 0.8 °C for the low moisture class (Fig. 10g; p-value <0.001). Previous studies have also shown that temperature can serve as a good indicator of moisture status in peatlands (Kameoka et al., 2021; Langhammer et al., 2024; Lendzioch et al., 2021). In line with this, the mean *VWC* and mean surface temperature over the study period are negatively and significantly correlated (−0.48; Table 5).

3.5. Possible applications of drone-borne GPR for peatland restoration initiatives

First, the spatial clustering of peatland moisture provides valuable information for identifying moisture patterns relevant to peatland restoration planning. Restoration efforts typically aim to re-establish high water levels (Holden et al., 2004). Given the high costs of restoration measures (Andersen et al., 2017), careful planning and appropriate selection of restoration sites are essential. Clustering based on drone-borne GPR maps can help identify drier zones needing more intensive restoration efforts, as well as wetter areas that do not require intervention. To this aim, the scale of the clusters map should match the management scale. In particular, small-scale classes (<20 m) should be removed to allow for a coherent, landscape-scale classification. The number of clusters considered should be adjusted according to the types of restoration strategies envisioned and the chosen thresholds for intervention.

This approach would be successful on this site because the resulting moisture classes are spatially homogeneous (ranging from 50 to 300 m, when excluding near-isolated pixels), simplifying targeted actions. Additionally, these moisture classes differ in factors like vegetation and peat depth, both indicators of peatland degradation status. For this site, distinct restoration strategies could be applied to the three moisture classes. Since the low moisture class is located on a slope, it is not the most suitable area for peatland development, and significant restoration efforts would likely not be effective there. However, moderate actions could still be implemented, such as removing conifer remnants to prevent their spread and blocking the ditches (using potential scarification products) to reduce rapid surface runoff. In the intermediate moisture class, particularly in areas with a high density of invasive *Molinia caerulea*, targeted restoration actions could be applied. A possible strategy would be to conduct topsoil removal (removing vegetation and the mineralized peat upper layer) to bring the water table closer to the surface and promote the appearance and growth of peat-forming vegetation (Frankard, 2004). In this case, the peat depth map (Fig. 9c) would serve as a complementary resource to avoid applying these restoration methods in the southeastern silty area, where it would be ineffective due to the too thin peat layer. Finally, the high moisture class likely requires no additional restoration, as its high water table naturally supports peat formation.

Second, monitoring root-zone moisture dynamics with drone-borne GPR can support the evaluation of temporal moisture responses following peatland restoration interventions. Andersen et al. (2017) highlighted the importance of establishing baselines for the assessment of restoration success. They recommended establishing systematic long-term monitoring techniques and developing new methods and proxies to study the changes in vegetation, hydrology and greenhouse gas fluxes. In this context, the drone-borne GPR approach could support evaluations of restoration success, as continuous moisture monitoring is essential for informing hydrological recovery. This method has indeed proven effective in monitoring overall temporal variations in moisture content over an area for more than a year, capturing the extent of *VWC* changes with a precision of less than 5 %. It is also performing well locally in unsaturated areas, which are the primary focus of restoration efforts. This approach enables both general monitoring of moisture content (e.g., assessing whether water content has increased as expected by the restoration efforts) and more specific temporal tracking (e.g., evaluating the impact of restoration on short-term moisture dynamics and potential drought sensitivity during specific periods). In this context, drone-based GPR is thus providing a non-invasive, rapid, relatively high-resolution alternative that fits between ground-based probes and satellite data, complementing the satellite-based methods proposed by Isoaho et al. (2024) for post-restoration moisture status monitoring.

4. Conclusion

This study aimed to explore the potential of drone-borne GPR, combined with full-wave inversion, for mapping and monitoring peatland moisture, a critical parameter for understanding global peatland conditions and informing restoration efforts. Below, we present the key conclusions corresponding to our four objectives followed by the perspectives.

(1) The methodology was successfully applied in a peatland and allowed the generation of 19 peatland root-zone moisture maps at a 5 m resolution across a 4.5 ha area over approximately one and a half years. This technique offers several advantages, including its non-destructive nature, speed, flexibility in measurement timing, and intermediate resolution that bridges the gap between ground-based probes and satellite imagery. It can be applied to peatlands with low vegetation (<4 m).
(2) The second objective was to evaluate whether drone-borne GPR could reliably monitor peatland root-zone moisture over time. Despite some limitations in highly waterlogged conditions, where only minor moisture variations occurred that were not sensed by the GPR, the method showed promising results, with an overall correlation over time of 0.71, comparable to or even surpassing previous approaches.
(3) The third objective was to assess the capability of drone-borne GPR to produce spatially accurate maps of root-zone moisture. While direct correlation over space with on-ground probes was low (0.23), this is likely due to high spatial variability of moisture in the study area, combined with differences in measurement scale and the fact that GPR and probe measurements were not exactly co-located. Despite this, the clustering analysis based on the GPR-derived maps allowed the delineation of moisture zones and revealed consistent large-scale spatial patterns that align well with other site characteristics, including peat depth, and vegetation types. Additionally, the mean GPR-derived *VWC* was significantly correlated with mean NDWI (0.42) and mean surface temperature (−0.48).
(4) Furthermore, this drone-borne GPR method could help support restoration initiatives in two ways. First, clustering can help identify specific locations (e.g., drier areas) for targeted peatland restoration measures. Second, temporal monitoring can be used to track changes in moisture after the interventions and assess their potential success.

These findings highlight the potential of drone-borne GPR for effective moisture spatial mapping and temporal monitoring, even in highly heterogeneous environments. Several improvements could still enhance its accuracy. These include ensuring more stable flight paths, reducing flight height, increasing measurement density for higher resolution, using differential GPS, adjusting for scale differences and co-location methods, filtering data based on kriging uncertainty, and accounting for changes in incidence angle. With these developments, the approach could offer enhanced precision in capturing complex moisture dynamics, supporting both research and targeted peatland restoration strategies. Further testing in other peatland types, including undisturbed reference sites, would help to confirm the broader applicability of this technique. Additionally, comparing this approach with more commonly used drone-based or satellite sensors in peatland studies could provide valuable insights into their relative effectiveness and potential synergies.

CRediT authorship contribution statement

Maud Henrion: Writing – original draft, Visualization, Methodology, Investigation, Formal analysis, Conceptualization. **Yanfei Li:** Writing – review & editing, Investigation. **Kaijun Wu:** Writing – review & editing, Methodology. **François Jonard:** Writing – review & editing, Funding acquisition. **Sophie Opfergelt:** Writing – review & editing, Funding acquisition. **Veerle Vanacker:** Writing – review & editing, Funding acquisition. **Kristof Van Oost:** Writing – review & editing, Funding acquisition, Conceptualization. **Sébastien Lambot:** Writing – review & editing, Software, Methodology, Funding acquisition, Conceptualization.

Declaration of generative AI and AI-assisted technologies in the writing process

During the preparation of this work the authors used ChatGPT in order to improve the readability and language of the manuscript. After using this tool, the authors reviewed and edited the content as needed and take full responsibility for the content of the published article.

Funding sources

This work is part of the Action de Recherche Concertée, LandSense project (n° 21/26–119), funded by the *Communauté française de Belgique*.

Declaration of competing interest

The authors declare that they have no known competing financial interests or personal relationships that could have appeared to influence the work reported in this paper.

Acknowledgments

Sophie Opfergelt, Kristof Van Oost, and Sébastien Lambot are supported by the *Fonds de la Recherche Scientifique* (FNRS). We thank the *Département de la Nature et des Forêts* (DNF), Manuel Lemaire and Joël Verdin for providing access to the study site. The development of gprSense® by Sébastien Lambot was funded by the agROBOfood project (MIRAGE, Grant Agreement No. 825395) and the ICAERUS project (gprSense®, Grant Agreement No. 101060643) through Open Calls supported by the European Union's Horizon Europe research and innovation program. We thank Adil Thami, Sébastien François, Florentin Bulliard and Gabriel Verbois for their help with fieldwork.

Data availability

The data used in this study are available at https://doi.org/10.5281/zenodo.16911685.
This includes:•
Point measurements of volumetric water content (*VWC*) derived from GPR after full-wave inversion and calibration, for the 2 zones across the 19 measurement dates•
Kriged *VWC* data derived from GPR after full-wave inversion, calibration, and kriging, for the 2 zones across the 19 measurement dates at a resolution of 5 m•
411 time-location *VWC* measurements using the CS615 ground-probe•
Calibrated *VWC* measurements from on-ground Teros12 sensors at 10 locations and two depths (10 and 30 cm), recorded every 10 min from May 2023 to September 2024

References

Ågren, A.M., Hasselquist, E.M., Stendahl, J., Nilsson, M.B., Paul, S.S., 2022. Delineating the distribution of mineral and peat soils at the landscape scale in northern boreal regions. SOIL 8, 733–749. https://doi.org/10.5194/soil-8-733-2022.
Ågren, A.M., Lidberg, W., Strömgren, M., Ogilvie, J., Arp, P.A., 2014. Evaluating digital terrain indices for soil wetness mapping – a Swedish case study. Hydrol. Earth Syst. Sci. 18, 3623–3634. https://doi.org/10.5194/hess-18-3623-2014.

Allan, J.M., Guêné-Nanchen, M., Rochefort, L., Douglas, D.J.T., Axmacher, J.C., 2024. Meta-analysis reveals that enhanced practices accelerate vegetation recovery during peatland restoration. Restor. Ecol. 32, e14015. https://doi.org/10.1111/rec.14015.
Andersen, R., Farrell, C., Graf, M., Muller, F., Calvar, E., Frankard, P., Caporn, S., Anderson, P., 2017. An overview of the progress and challenges of peatland restoration in Western Europe. Restor. Ecol. 25, 271–282. https://doi.org/10.1111/rec.12415.
Asmuß, T., Bechtold, M., Tiemeyer, B., 2019. On the potential of Sentinel-1 for high resolution monitoring of water table dynamics in grasslands on organic soils. Remote Sens. 11, 1659. https://doi.org/10.3390/rs11141659.
Bechtold, M., Schlaffer, S., Tiemeyer, B., De Lannoy, G., 2018. Inferring water table depth dynamics from ENVISAT-ASAR C-Band backscatter over a range of peatlands from deeply-drained to natural conditions. Remote Sens. 10, 536. https://doi.org/10.3390/rs10040536.
Bettink, K., 2009. Sharp Rush Juncus Acutus: Draft Strategic Plan for the Swan NRM Region.
Beven, K.J., Kirkby, M.J., 1979. A physically based, variable contributing area model of basin hydrology/Un modèle à base physique de zone d'appel variable de l'hydrologie du bassin versant. Hydrol. Sci. Bull. 24, 43–69. https://doi.org/10.1080/02626667909491834.
Bourgault, M.-A., Larocque, M., Garneau, M., 2019. How do hydrogeological setting and meteorological conditions influence water table depth and fluctuations in ombrotrophic peatlands? J. Hydrol. X 4. https://doi.org/10.1016/j.hydroa.2019.100032.
Bragazza, L., 2006. A decade of plant species changes on a mire in the Italian alps: vegetation-controlled or climate-driven mechanisms? Clim. Change 77, 415–429. https://doi.org/10.1007/s10584-005-9034-x.
Bragazza, L., Bardgett, R.D., Mitchell, E.A.D., Buttler, A., 2015. Linking soil microbial communities to vascular plant abundance along a climate gradient. New Phytol. 205, 1175–1182. https://doi.org/10.1111/nph.13116.
Brocca, L., Morbidelli, R., Melone, F., Moramarco, T., 2007. Soil moisture spatial variability in experimental areas of central Italy. J. Hydrol. 333, 356–373. https://doi.org/10.1016/j.jhydrol.2006.09.004.
Burdun, I., Bechtold, M., Aurela, M., De Lannoy, G., Desai, A.R., Humphreys, E., Kareksela, S., Komisarenko, V., Liimatainen, M., Marttila, H., Minkkinen, K., Nilsson, M.B., Ojanen, P., Salko, S.-S., Tuittila, E.-S., Uuemaa, E., Rautiainen, M., 2023. Hidden becomes clear: optical remote sensing of vegetation reveals water table dynamics in northern peatlands. Rem. Sens. Environ. 296, 113736. https://doi.org/10.1016/j.rse.2023.113736.
Burdun, I., Bechtold, M., Sagris, V., Komisarenko, V., De Lannoy, G., Mander, Ü., 2020. A comparison of three trapezoid models using optical and thermal satellite imagery for water table depth monitoring in Estonian bogs. Remote Sens. 12, 1980. https://doi.org/10.3390/rs12121980.
Cheng, M., Jiao, X., Liu, Y., Shao, M., Yu, X., Bai, Y., Wang, Z., Wang, S., Tuohuti, N., Liu, S., Shi, L., Yin, D., Huang, X., Nie, C., Jin, X., 2022. Estimation of soil moisture content under high maize canopy coverage from UAV multimodal data and machine learning. Agric. Water Manag. 264, 107530. https://doi.org/10.1016/j.agwat.2022.107530.
Cheng, Q., Su, Q., Binley, A., liu, J., Zhang, Z., Chen, X., 2023. Estimation of surface soil moisture by a multi-elevation UAV-Based ground penetrating radar. Water Resour. Res. 59. https://doi.org/10.1029/2022WR032621.
de Lima, R.S., Li, K.-Y., Vain, A., Lang, M., Bergamo, T.F., Kokamägi, K., Burnside, N.G., Ward, R.D., Sepp, K., 2022. The potential of optical UAS data for predicting surface soil moisture in a peatland across time and sites. Remote Sens. 14, 2334. https://doi.org/10.3390/rs14102334.
Ding, R., Jin, H., Xiang, D., Wang, Xiaocheng, Zhang, Y., Shen, D., Su, L., Hao, W., Tao, M., Wang, Xinbing, Zhou, C., 2023. Soil moisture sensing with UAV-mounted IR-UWB radar and deep learning. Proc. ACM Interact. Mob. Wearable Ubiquitous Technol. 7. https://doi.org/10.1145/3580867.
European Commission, 2021. European Missions - a Soil Deal for Europe - Implementation Plan.
Frankard, P., 2004. Bilan de 12 années de gestion conservatoire des tourbières hautes dans la réserve naturelle domaniale des Hautes-Fagnes (Est de la Belgique). Géocarrefour 79, 269–276. https://doi.org/10.4000/geocarrefour.795.
Frankard, P., Ghiette, P., Hindryckx, M.-N., Schumaker, R., Wastiaux, C., 1998. Peatlands of wallony (S-Belgium). Suo: Mires Peat 49, 33–47.
Galagedara, L.W., Parkin, G.W., Redman, J.D., 2003. An analysis of the ground-penetrating radar direct ground wave method for soil water content measurement. Hydrol. Process. 17, 3615–3628. https://doi.org/10.1002/hyp.1351.
Gatis, N., Luscombe, D.J., Grand-Clement, E., Hartley, I.P., Anderson, K., Smith, D., Brazier, R.E., 2016. The effect of drainage ditches on vegetation diversity and CO_2 fluxes in a *Molinia caerulea* -dominated peatland. Ecohydrology 9, 407–420. https://doi.org/10.1002/eco.1643.
Ghazaryan, G., Krupp, L., Seyfried, S., Landgraf, N., Nendel, C., 2024. Enhancing peatland monitoring through multisource remote sensing: optical and radar data applications. Int. J. Rem. Sens. 45, 6372–6394. https://doi.org/10.1080/01431161.2024.2387133.
Goemaere, E., Demarque, S., Dreesen, R., Declercq, P.-Y., 2016. The geological and cultural heritage of the caledonian stavelot-venn massif, Belgium. Geoheritage 8, 211–233. https://doi.org/10.1007/s12371-015-0155-y.
Goetz, S.J., 1997. Multi-sensor analysis of NDVI, surface temperature and biophysical variables at a mixed grassland site. Int. J. Rem. Sens. 18, 71–94. https://doi.org/10.1080/014311697219286.
González, E., Rochefort, L., Boudreau, S., Poulin, M., 2014. Combining indicator species and key environmental and management factors to predict restoration success of degraded ecosystems. Ecol. Indic. 46, 156–166. https://doi.org/10.1016/j.ecolind.2014.06.016.
Gorham, E., Rochefort, L., 2003. Peatland restoration: a brief assessment with special reference to sphagnum bogs. Wetl. Ecol. Manag. 11, 109–119.
Gu, Y., Hunt, E., Wardlow, B., Basara, J.B., Brown, J.F., Verdin, J.P., 2008. Evaluation of MODIS NDVI and NDWI for vegetation drought monitoring using Oklahoma mesonet soil moisture data. Geophys. Res. Lett. 35. https://doi.org/10.1029/2008GL035772.
Hasan, A., Pilesjö, P., Persson, A., 2012. On generating digital elevation models from lidar data - resolution versus accuracy and topographic wetness indices in northern peatlands. Geod. Cartogr. 38, 57–69. https://doi.org/10.3846/20296991.2012.702983.
Henrion, M., Li, Y., Koganti, T., Bechtold, M., Jonard, F., Opfergelt, S., Vanacker, V., Van Oost, K., Lambot, S., 2024. Mapping and monitoring peatlands in the Belgian Hautes Fagnes: insights from ground-penetrating radar and electromagnetic induction characterization. Geoderma Regional 37. https://doi.org/10.1016/j.geodrs.2024.e00795.
Holden, J., 2006. Chapter 14 peatland hydrology. In: Peatlands: Evolution and Records of Environmental and Climate Changes, Developments in Earth Surface Processes. Elsevier, pp. 319–346. https://doi.org/10.1016/S0928-2025(06)09014-6.
Holden, J., Chapman, P.J., Labadz, J.C., 2004. Artificial drainage of peatlands: hydrological and hydrochemical process and wetland restoration. Prog. Phys. Geogr. 28, 95–123. https://doi.org/10.1191/0309133304pp403ra.
Hrysiewicz, A., Holohan, E.P., Donohue, S., Cushnan, H., 2023. SAR and InSAR data linked to soil moisture changes on a temperate raised peatland subjected to a wildfire. Rem. Sens. Environ. 291, 113516. https://doi.org/10.1016/j.rse.2023.113516.
Huisman, J.A., Hubbard, S.S., Redman, J.D., Annan, A.P., 2003. Measuring soil water content with ground penetrating radar: a review. Vadose Zone J. 2, 476–491.
Ikkala, L., Ronkanen, A.-K., Ilmonen, J., Similä, M., Rehell, S., Kumpula, T., Päkkilä, L., Klöve, B., Marttila, H., 2022. Unmanned Aircraft System (UAS) structure-from-motion (SfM) for monitoring the changed flow paths and wetness in minerotrophic peatland restoration. Remote Sens. 14, 3169. https://doi.org/10.3390/rs14133169.
Isoaho, A., Ikkala, L., Marttila, H., Hjort, J., Kumpula, T., Korpelainen, P., Räsänen, A., 2023. Spatial water table level modelling with multi-sensor unmanned aerial vehicle data in boreal aapa mires. Remote Sens. Appl.: Society and Environment 32, 101059. https://doi.org/10.1016/j.rsase.2023.101059.
Isoaho, A., Ikkala, L., Päkkilä, L., Marttila, H., Kareksela, S., Räsänen, A., 2024. Multi-sensor satellite imagery reveals spatiotemporal changes in peatland water table after restoration. Rem. Sens. Environ. 306, 114144. https://doi.org/10.1016/j.rse.2024.114144.
Jacome, A., Bernier, M., Chokmani, K., Gauthier, Y., Poulin, J., De Sève, D., 2013. Monitoring Volumetric Surface Soil Moisture Content at the La Grande Basin Boreal Wetland by Radar Multi Polarization Data. Remote Sens. 5, 4919–4941. https://doi.org/10.3390/rs5104919.
Jonard, F., Andre, F., Pinel, N., Warren, C., Vereecken, H., Lambot, S., 2019. Modeling of multilayered media green's functions with rough interfaces. IEEE Trans. Geosci. Rem. Sens. 57, 7671–7681. https://doi.org/10.1109/TGRS.2019.2915676.
Jonard, F., Weihermüller, L., Vereecken, H., Lambot, S., 2012. Accounting for soil surface roughness in the inversion of ultrawideband off-ground GPR signal for soil moisture retrieval. Geophysics 77, H1–H7. https://doi.org/10.1190/geo2011-0054.1.
Kalacska, M., Arroyo-Mora, J.P., Soffer, R.J., Roulet, N.T., Moore, T.R., Humphreys, E., Leblanc, G., Lucanus, O., Inamdar, D., 2018. Estimating peatland water table depth and net ecosystem exchange: a comparison between satellite and airborne imagery. Remote Sens. 10, 687. https://doi.org/10.3390/rs10050687.
Kameoka, T., Kozan, O., Hadi, S., Asnawi, Hasrullah, 2021. Monitoring the groundwater level in tropical peatland through UAV mapping of soil surface temperature: a pilot study in Tanjung leban, Indonesia. Remote Sensing Letters 12, 542–552. https://doi.org/10.1080/2150704X.2021.1906974.
Kechavarzi, C., Dawson, Q., Bartlett, M., Leeds-Harrison, P.B., 2010. The role of soil moisture, temperature and nutrient amendment on CO2 efflux from agricultural peat soil microcosms. Geoderma 154, 203–210. https://doi.org/10.1016/j.geoderma.2009.02.018.
Kelleners, T.J., Seyfried, M.S., Blonquist, J.M., Bilskie, J., Chandler, D.G., 2005. Improved interpretation of water content reflectometer measurements in soils. SSSA (Soil Sci. Soc. Am.) J. 69, 1684–1690. https://doi.org/10.2136/sssaj2005.0023.
Kellner, E., Lundin, L.-C., 2001. Calibration of time domain reflectometry for water content in peat soil. Nordic Hydrology 32, 315–332. https://doi.org/10.2166/nh.2001.0018.
Klinke, R., Kuechly, H., Frick, A., Förster, M., Schmidt, T., Holtgrave, A.-K., Kleinschmit, B., Spengler, D., Neumann, C., 2018. Indicator-based soil moisture monitoring of wetlands by utilizing sentinel and landsat remote sensing data. Photogramm. Fernerkund. GeoInf. 86, 71–84. https://doi.org/10.1007/s41064-018-0044-5.
Klotzsche, A., Jonard, F., Looms, M.C., van der Kruk, J., Huisman, J.A., 2018. Measuring soil water content with ground penetrating radar: a decade of progress. Vadose Zone J. 17, 180052. https://doi.org/10.2136/vzj2018.03.0052.
Kreyling, J., Tanneberger, F., Jansen, F., van der Linden, S., Aggenbach, C., Blüml, V., Couwenberg, J., Emsens, W.-J., Joosten, H., Klimkowska, A., Kotowski, W., Kozub, L., Lennartz, B., Liczner, Y., Liu, H., Michaelis, D., Oehmke, C., Parakenings, K., Pleyl, E., Poyda, A., Raabe, S., Röhl, M., Rücker, K., Schneider, A., Schrautzer, J., Schröder, C., Schug, F., Seeber, E., Thiel, F., Thiele, S., Tiemeyer, B., Timmermann, T., Urich, T., van Diggelen, R., Vegelin, K., Verbruggen, E., Wilmking, M., Wrage-Mönnig, N., Wołejko, L., Zak, D., Jurasinski, G., 2021. Rewetting does not return drained fen peatlands to their old selves. Nat. Commun. 12, 5693. https://doi.org/10.1038/s41467-021-25619-y.

Lambot, S., Andre, F., 2014. Full-wave modeling of near-field radar data for planar layered media reconstruction. IEEE Trans. Geosci. Rem. Sens. 52, 2295–2303. https://doi.org/10.1109/TGRS.2013.2259243.

Lambot, S., Slob, E.C., van den Bosch, I., Stockbroeckx, B., Scheers, B., Vanclooster, M., 2004a. Estimating soil electric properties from monostatic ground-penetrating radar signal inversion in the frequency domain. Water Resour. Res. 40, 2003WR002095. https://doi.org/10.1029/2003WR002095.

Lambot, S., Slob, E.C., van den Bosch, I., Stockbroeckx, B., Vanclooster, M., 2004b. Modeling of ground-penetrating radar for accurate characterization of subsurface electric properties. IEEE Trans. Geosci. Rem. Sens. 42, 2555–2568. https://doi.org/10.1109/TGRS.2004.834800.

Lambot, S., Weihermüller, L., Huisman, J.A., Vereecken, H., Vanclooster, M., Slob, E.C., 2006. Analysis of air-launched ground-penetrating radar techniques to measure the soil surface water content. Water Resour. Res. 42, W11403. https://doi.org/10.1029/2006WR005097.

Langhammer, J., Lendzioch, T., Vlček, L., 2024. Montane peatland response to drought: evidence from multispectral and thermal UAS monitoring. Ecol. Indic. 167, 112587. https://doi.org/10.1016/j.ecolind.2024.112587.

Lees, K.J., Artz, R.R.E., Chandler, D., Aspinall, T., Boulton, C.A., Buxton, J., Cowie, N.R., Lenton, T.M., 2021. Using remote sensing to assess peatland resilience by estimating soil surface moisture and drought recovery. Sci. Total Environ. 761. https://doi.org/10.1016/j.scitotenv.2020.143312.

Lees, K.J., Artz, R.R.E., Khomik, M., Clark, J.M., Ritson, J., Hancock, M.H., Cowie, N.R., Quaife, T., 2020. Using spectral indices to estimate water content and GPP in *sphagnum* moss and other peatland vegetation. IEEE Trans. Geosci. Rem. Sens. 58, 4547–4557. https://doi.org/10.1109/TGRS.2019.2961479.

Lendzioch, T., Langhammer, J., Vlček, L., Minařík, R., 2021. Mapping the groundwater level and soil moisture of a montane peat bog using UAV monitoring and machine learning. Remote Sens. 13. https://doi.org/10.3390/rs13050907.

Li, Y., Henrion, M., Moore, A., Lambot, S., Opfergelt, S., Vanacker, V., Jonard, F., Van Oost, K., 2025. Hotspots, hot moments, and spatiotemporal drivers of soil CO_2 flux in temperate peatlands using UAV remote sensing. EGUsphere. https://doi.org/10.5194/egusphere-2025-1595 [preprint].

Li, Y., Henrion, M., Moore, A., Lambot, S., Opfergelt, S., Vanacker, V., Jonard, F., Van Oost, K., 2024. Factors controlling peat soil thickness and carbon storage in temperate peatlands based on UAV high-resolution remote sensing. Geoderma 449, 117009. https://doi.org/10.1016/j.geoderma.2024.117009.

Linkevičienė, R., Šimanauskienė, R., Kibirkštis, G., Grigaitė, O., Taminskas, J., 2023. Hydrological and botanical diversity of a raised bog and its evaluation using in situ and remote sensing methods. J. Hydrol. 617, 129119. https://doi.org/10.1016/j.jhydrol.2023.129119.

McFeeters, S.K., 1996. The use of the Normalized Difference Water Index (NDWI) in the delineation of open water features. Int. J. Rem. Sens. 17, 1425–1432. https://doi.org/10.1080/01431169608948714.

Meingast, K.M., Falkowski, M.J., Kane, E.S., Potvin, L.R., Benscoter, B.W., Smith, A.M.S., Bourgeau-Chavez, L.L., Miller, M.E., 2014. Spectral detection of near-surface moisture content and water-table position in northern peatland ecosystems. Rem. Sens. Environ. 152, 536–546. https://doi.org/10.1016/j.rse.2014.07.014.

Menberu, M.W., Tahvanainen, T., Marttila, H., Irannezhad, M., Ronkanen, A., Penttinen, J., Kløve, B., 2016. Water-table-dependent hydrological changes following peatland forestry drainage and restoration: analysis of restoration success. Water Resour. Res. 52, 3742–3760. https://doi.org/10.1002/2015WR018578.

Minasny, B., Adetsu, D.V., Aitkenhead, M., Artz, R.R.E., Baggaley, N., Barthelmes, A., Beucher, A., Caron, J., Conchedda, G., Connolly, J., Deragon, R., Evans, C., Fadnes, K., Fiantis, D., Gagkas, Z., Gilet, L., Gimona, A., Glatzel, S., Greve, M.H., Habib, W., Hergoualc'h, K., Hermansen, C., Kidd, D.B., Koganti, T., Kopansky, D., Large, D.J., Larmola, T., Lilly, A., Liu, H., Marcus, M., Middleton, M., Morrison, K., Petersen, R.J., Quaife, T., Rochefort, L., Rudiyanto, Toca, L., Tubiello, F.N., Weber, P.L., Weldon, S., Widyatmanti, W., Williamson, J., Zak, D., 2023. Mapping and monitoring peatland conditions from global to field scale. Biogeochemistry. https://doi.org/10.1007/s10533-023-01084-1.

Minet, J., Bogaert, P., Vanclooster, M., Lambot, S., 2012. Validation of ground penetrating radar full-waveform inversion for field scale soil moisture mapping. J. Hydrol. 424–425, 112–123.

Noviello, C., Gennarelli, G., Esposito, G., Ludeno, G., Fasano, G., Capozzoli, L., Soldovieri, F., Catapano, I., 2022. An overview on down-looking UAV-based GPR systems. Remote Sens. 14. https://doi.org/10.3390/rs14143245.

Pathirana, S., Lambot, S., Krishnapillai, M., Cheema, M., Smeaton, C., Galagedara, L., 2023. Ground-penetrating radar and electromagnetic induction: challenges and opportunities in agriculture. Remote Sens. 15, 2932. https://doi.org/10.3390/rs15112932.

Pepin, S., Plamondon, A., Stein, J., 1992. Peat water content measurement using time domain reflectometry. Can. J. For. Res. 22, 534–540.

Petrone, R.M., Price, J.S., Carey, S.K., Waddington, J.M., 2004. Statistical characterization of the spatial variability of soil moisture in a cutover peatland. Hydrol. Process. 18, 41–52. https://doi.org/10.1002/hyp.1309.

Pramudita, A.A., Wahyu, Y., Rizal, S., Prasetio, M.D., Jati, A.N., Wulansari, R., Ryanu, H. H., 2022. Soil water content estimation with the presence of vegetation using ultra wideband radar-drone. IEEE Access 10, 85213–85227. https://doi.org/10.1109/ACCESS.2022.3197636.

Price, J., 1997. Soil moisture, water tension, and water table relationships in a managed cutover bog. J. Hydrol. 202, 21–32. https://doi.org/10.1016/S0022-1694(97)00037-1.

Räsänen, A., Virtanen, T., 2019. Data and resolution requirements in mapping vegetation in spatially heterogeneous landscapes. Rem. Sens. Environ. 230, 111207. https://doi.org/10.1016/j.rse.2019.05.026.

Reiniger, P., Seguin, B., 1986. Surface temperature as an indicator of evapotranspiration and soil moisture. Remote Sens. Rev. 1, 277–310. https://doi.org/10.1080/02757258609532071.

Rosenbaum, U., Bogena, H.R., Herbst, M., Huisman, J.A., Peterson, T.J., Weuthen, A., Western, A.W., Vereecken, H., 2012. Seasonal and event dynamics of spatial soil moisture patterns at the small catchment scale. Water Resour. Res. 48. https://doi.org/10.1029/2011wr011518.

Saarikoski, H., Mustajoki, J., Hjerppe, T., Aapala, K., 2019. Participatory multi-criteria decision analysis in valuing peatland ecosystem services—Trade-offs related to peat extraction vs. pristine peatlands in Southern Finland. Ecol. Econ. 162, 17–28. https://doi.org/10.1016/j.ecolecon.2019.04.010.

Sadeghi, M., Babaeian, E., Tuller, M., Jones, S.B., 2017. The optical trapezoid model: a novel approach to remote sensing of soil moisture applied to Sentinel-2 and Landsat-8 observations. Rem. Sens. Environ. 198, 52–68. https://doi.org/10.1016/j.rse.2017.05.041.

Sandholt, I., Rasmussen, K., Andersen, J., 2002. A simple interpretation of the surface temperature/vegetation index space for assessment of surface moisture status. Rem. Sens. Environ. 79, 213–224. https://doi.org/10.1016/S0034-4257(01)00274-7.

Šimanauskienė, R., Linkevičienė, R., Bartold, M., Dąbrowska-Zielińska, K., Slavinskienė, G., Veteikis, D., Taminskas, J., 2019. Peatland degradation: the relationship between raised bog hydrology and normalized difference vegetation index. Ecohydrology 12, e2159. https://doi.org/10.1002/eco.2159.

Sun, J., Gallego-Sala, A., Yu, Z., 2023. Topographic and climatic controls of peatland distribution on the Tibetan Plateau. Sci. Rep. 13, 14811. https://doi.org/10.1038/s41598-023-39699-x.

Topp, G.C., Davis, J.L., 1985. Measurement of soil water content using time-domain reflectometry (TDR): a field evaluation. SSSA (Soil Sci. Soc. Am.) J. 49, 19–24. https://doi.org/10.2136/sssaj1985.03615995004900010003x.

UNEP, 2022. Global peatlands assessment: the state of the world's peatlands - evidence for action toward the conservation, restoration, and sustainable management of peatlands. United Nations Environment Programme. https://doi.org/10.59117/20.500.11822/41222.

Waddington, J.M., Morris, P.J., Kettridge, N., Granath, G., Thompson, D.K., Moore, P.A., 2015. Hydrological feedbacks in northern peatlands. Ecohydrology 8, 113–127. https://doi.org/10.1002/eco.1493.

Wang, M., Liu, H., Lennartz, B., 2021. Small-scale spatial variability of hydro-physical properties of natural and degraded peat soils. Geoderma 399, 115123. https://doi.org/10.1016/j.geoderma.2021.115123.

Wastiaux, C., 2008. Les tourbières sont-elles des éponges régularisant l'écoulement. Bulletin de la Société géographique de Liège 50, 57–66.

Western, A.W., Blöschl, G., 1999. On the spatial scaling of soil moisture. J. Hydrol. 217, 203–224. https://doi.org/10.1016/S0022-1694(98)00232-7.

Wigmore, O., Mark, B., McKenzie, J., Baraer, M., Lautz, L., 2019. Sub-metre mapping of surface soil moisture in proglacial valleys of the tropical andes using a multispectral unmanned aerial vehicle. Rem. Sens. Environ. 222, 104–118. https://doi.org/10.1016/j.rse.2018.12.024.

Wijewardana, Y.G.N.S., Galagedara, L.W., 2010. Estimation of spatio-temporal variability of soil water content in agricultural fields with ground penetrating radar. J. Hydrol. 391, 24–33. https://doi.org/10.1016/j.jhydrol.2010.06.036.

Wu, K., Artois, J., Tourneur, D., Mareschal, M., Henrion, M., Pathirana, S., Galagedara, L., Limbourg, Q., Lambot, S., 2025. Drone-borne GPR reveals dynamic root-zone moisture patterns for optimized irrigation. Rem. Sens. Environ. https://doi.org/10.2139/ssrn.5148563 [preprint].

Wu, K., Lambot, S., 2022a. Effect of radar incident angle on full-wave inversion for the retrieval of medium surface permittivity for drone-borne applications. IEEE Trans. Geosci. Rem. Sens. 60, 4508710. https://doi.org/10.1109/TGRS.2022.3157370.

Wu, K., Lambot, S., 2022b. Analysis of low-frequency drone-borne GPR for root-zone soil electrical conductivity characterization. IEEE Trans. Geosci. Rem. Sens. 60, 2006213. https://doi.org/10.1109/TGRS.2022.3198431.

Wu, K., Rodriguez, G.A., Zajc, M., Jacquemin, E., Clément, M., De Coster, A., Lambot, S., 2019. A new drone-borne GPR for soil moisture mapping. Rem. Sens. Environ. 235, 111456. https://doi.org/10.1016/j.rse.2019.111456.

Zhang, W., Lu, Q., Song, K., Qin, G., Wang, Y., Wang, X., Li, Hongxia, Li, J., Liu, G., Li, Hua, 2014. Remotely sensing the ecological influences of ditches in Zoige Peatland, eastern Tibetan Plateau. Int. J. Rem. Sens. 35, 5186–5197. https://doi.org/10.1080/01431161.2014.939779.